Research Square

Preprints are preliminary reports that have not undergone peer review.
They should not be considered conclusive, used to inform clinical practice,
or referenced by the media as validated information.

GC-MS Based Phytochemical Profiling and Integrated In vitro and In silico Evaluation of Cucurbita maxima Leaf Extract Against Diabetes and Androgen Receptor Dependent Prostate Cancer

Sozoni Khatun
Islamic University
Md. Jubel Hussein
Islamic University
Md Reduanul Haque Kavey
Islamic University
Md Jannatul Islam Polash
Islamic University
Md Anisur Rahman
Islamic University
Tasfia Saffat
Islamic University
Israt Jahan
Islamic University
Talha Jobayer Rifat
Pabna University of Science and Technology
Mohammad Ali
Khwaja Yunus Ali University
Md. Maruf Hossen
Khwaja Yunus Ali University
Md. Abdullah Al Mashud
Islamic University
Arghya Prosun Sarkar
arghya@pharmacy.iu.ac.bd

Islamic University

Article

Keywords: Androgen receptor dependent prostate cancer, Diabetes, GC-MS, Docking, Molecular Dynamic Simulation

Posted Date: November 2nd, 2026

DOI: https://doi.org/10.21203/rs.3.rs-11109689/v1

License: This work is licensed under a Creative Commons Attribution 4.0 International License.
Read Full License

Additional Declarations: No competing interests reported.

GC-MS Based Phytochemical Profiling and Integrated In vitro and In silico Evaluation of Cucurbita maxima Leaf Extract Against Diabetes and Androgen Receptor Dependent Prostate Cancer

Sozoni Khatun[1,5], Md.Jubel Hussein[1], Md Reduanul Haque Kavey[1], Md Jannatul Islam Polash[1], Md Anisur Rahman[1], Tasfia Saffat[1], Israt Jahan[1], Talha Jobayer Rifat[2], Mohammad Ali[3], Md. Maruf Hossen[3], Md. Abdullah Al Mashud[4,5] and Arghya Prosun Sarkar[1,5]

[1]Department of Pharmacy, Islamic University, Kushtia, Bangladesh.
[2]Drpartment of Pharmacy, Pabna University of Science and Technology.
[3]Department of Pharmacy,Khwaja Yunus Ali University, Enayetpur, Sirajganj, Rajshahi.
[4]Biophysics and Biomedicine Research Lab, Department of Electrical and Electronic Engineering, Islamic University, Kushtia-7003, Bangladesh.
[5]Greenford Nano and Cancer Foundation, Kushtia-7000, Bangladesh.

Correspondence: *Arghya Prosun Sarkar (Email: arghya@pharmacy.iu.ac.bd), Md. Abdullah Al Mashud (mashud.eap@gmail.com)*

Abstract

Prostate cancer and diabetes mellitus pose significant therapeutic problems, highlighting the need for new bioactive substances that might alter both metabolic and oncogenic pathways. In this study, we evaluated the α-amylase inhibitory activity of a plant-derived sample and investigated its binding efficacy against a diabetes-related target and androgen receptor using molecular docking and molecular dynamics (MD) simulations. The sample demonstrated concentration-dependent α-amylase inhibition, with inhibitory activity increasing from 11.44 ± 6.17% at 1.25 mg/mL to 68.32 ± 0.17% at 10 mg/mL, corresponding to an estimated IC_{50} value of 5.27 mg/mL compared with 3.50 mg/mL for the reference standard. Molecular docking of 147 compounds identified several favorable ligand–target interactions. For the diabetes-related target, Vitamin k1(20),heptafluorobutyric derive (CMP148) exhibited the highest predicted binding affinity (−9.8 kcal/mol), followed by Stigmasterol (CMP88) (−8.9 kcal/mol), both of which surpassed the predicted binding affinity of acarbose (−7.7 kcal/mol). Against the androgen receptor, CMP88 and Desmosterol (CMP91) showed strong binding affinities of −8.6 and −8.5 kcal/mol, respectively, outperforming reference drugs abiraterone (−8.1 kcal/mol) and bicalutamide (−7.7

kcal/mol). Subsequent 100-ns MD simulations demonstrated generally stable protein–ligand complexes, with RMSD values consistently below 3 Å. CMP88 exhibited optimal dynamic stability for the diabetes-related target, yielding MM/GBSA binding energies of −32.52, −34.86, and −30.97 kJ/mol across evaluated time points. For the androgen receptor, CMP91 displayed the strongest dynamic profile, featuring a mean RMSD of 1.267 ± 0.147 Å and an MM/GBSA binding energy of −35.35 kJ/mol at 50 ns. These finding demonstrate concentration dependent α – amylase inhibition and highlight CMP88 and CMP91 as promising candidates for the diabetes-related and androgen receptor targets, respectively, requiring additional biochemical and cellular confirmation.

Keywords: *Androgen receptor dependent prostate cancer, Diabetes, GC-MS, Docking, Molecular Dynamic Simulation*

1. Introduction

Diabetes mellitus and prostate cancer are major chronic diseases that continue to impose substantial health burdens worldwide. Diabetes mellitus, particularly type 2 diabetes, is characterized by a progressive interplay between insulin resistance and β-cell dysfunction, ultimately leading to persistent hyperglycemia and an increased risk of long-term complications [1,2]. Prostate cancer remains one of the most commonly diagnosed cancers among men worldwide. In 2022, it accounted for approximately 1.5 million new cases globally, representing 7.3% of all newly diagnosed cancers, and was the second most frequently diagnosed cancer worldwide and a major cause of cancer-related mortality among men [3]. The substantial and persistent burden of both diseases highlights the need to explore additional therapeutic leads with complementary mechanisms of action.

The pharmacological management of diabetes involves multiple glucose-lowering drug classes, selected according to glycemic efficacy, comorbidities, adverse effects, and individual patient characteristics [1]. Although widely used, some conventional antidiabetic agents are associated with treatment-related adverse effects that may affect tolerability and adherence [4]. Regulation of postprandial blood glucose therefore represents an important therapeutic consideration. In this context, pancreatic α-amylase is a relevant molecular target because it catalyzes the hydrolysis of

dietary starch into smaller carbohydrates, and its inhibition can reduce the rapid release and absorption of glucose following carbohydrate ingestion [5]. Accordingly, inhibition of α-amylase and other carbohydrate-digesting enzymes has been investigated as a strategy for controlling postprandial hyperglycemia [5–7]. In addition, oxidative stress is closely associated with type 2 diabetes and its complications, providing a biological rationale for evaluating antioxidant activity alongside antidiabetic-relevant effects [8].

In prostate cancer, androgen receptor (AR) signaling plays a central role in regulating the growth, survival, and progression of prostate cancer cells [9]. Androgen-deprivation therapy and AR-directed approaches remain important components of prostate cancer management; however, treatment-related adverse effects and the eventual development of castration-resistant disease and resistance to AR-targeted therapies remain major therapeutic challenges [10]. These limitations have encouraged continued investigation of new molecular scaffolds capable of modulating AR-associated signaling. Natural products are particularly attractive in drug discovery because they provide structurally diverse chemical scaffolds and a broad range of biologically active molecules [11]. Recent evidence further indicates that naturally derived compounds can modulate AR signaling in prostate cancer models, supporting their potential as sources of lead compounds for prostate cancer research [12].

Cucurbita maxima Duchesne (Cucurbitaceae), commonly known as pumpkin, is an important edible plant cultivated in Bangladesh. Although its fruits and seeds have received considerable scientific attention, its leaves remain comparatively less investigated. Previous characterization of different edible portions of *C. maxima* demonstrated that the leaves contain phenolic compounds, flavonoids, carotenes, minerals, and other potentially bioactive constituents, together with measurable antioxidant activity, suggesting that the leaves may represent a valuable source of nutraceutically relevant compounds [13]. Moreover, an earlier *in vitro* study specifically demonstrated DPPH radical-scavenging and pancreatic α-amylase inhibitory activities of the methanolic leaf extract of *C. maxima*, providing preliminary evidence for its antioxidant and antidiabetic-relevant potential [14]. These findings establish a rationale for further investigation of the chemical composition and biological properties of *C. maxima* leaves.

Despite these observations, the chemical constituents underlying the biological activities of *C. maxima* leaves remain incompletely characterized, particularly in relation to extraction solvent and their potential interactions with therapeutically relevant molecular targets. An integrated approach combining comparative extraction, phytochemical profiling, biochemical evaluation, and molecular docking may therefore provide complementary evidence linking extract composition with observed biological activities and predicted target interactions.

Accordingly, the present study comparatively evaluated methanolic leaf extracts of *C. maxima* for pancreatic α-amylase inhibitory activities. GC–MS analysis was subsequently performed to characterize the phytochemical constituents of the extracts, while molecular docking was employed to investigate the potential interactions of identified compounds with human pancreatic α-amylase and the androgen receptor. By integrating chemical profiling, *in vitro* biological assays, and target-oriented *in silico* analysis, this study aimed to identify potentially bioactive constituents of *C. maxima* leaves and provide preliminary mechanistic insights into their relevance to antidiabetic and AR-driven prostate cancer research.

2. Materials and Methods The leaves of *Cucurbita maxima* were collected from a home garden in Bheramara, Kushtia, Bangladesh, and authenticated by a botanist (Accession No. 10343)

2.1 Preparation of Plant Material

At first, the fresh leaves of *Cucurbita maxima* were collected from a home garden in Bheramara, Kushtia, Bangladesh and authenticated by a botanist (Accession No. 10343). Then the mature fresh leaves of *Cucurbita maxima* were washed separately in clean water thoroughly 2–3 times and once finally with sterile water to remove adhering dust. The leaves were sun dried under shade, then dried in the oven at 65°C and then powdered in a mixture grinder. About 250g of the plant leaves extract was weighed separately and placed into beaker with 500ml of methanol and ethyl acetate, respectively by cold maceration for 48 hours. The mixtures were then filtered and concentrated under reduced pressure in a rotary evaporator at 64°C and 77°C for methanolic and ethyl acetate extract respectively. The resulting extracts were collected and stored at 4 °C in a refrigerator [15].

2.2 Gas Chromatography-Mass Spectrometry (GC-MS) Analysis

The leaves of *Cucurbita maxima* were analyzed using Gas Chromatography-Mass Spectrometry and this study was performed by BCSIR, 1205, Dhaka, Bangladesh.

2.3 Alpha-Amylase Inhibition Assay (*In Vitro*)

2.3.1 DNSA Method

This experiment was carried out using a modified procedure. A tube containing 250 µL of extract (1.25, 2.5, 5, and 10 mg/mL) was mixed with 250 µL of 0.02M sodium phosphate buffer (pH 6.9) and alpha amylase solution (0.5 mg/ml). Pre incubation was carried out at 250°C for 10 minutes and 250 µL of 1% starch solution in 0.02M sodium phosphate buffer (pH 6.9) was added at intervals and further incubated at 250°C for 10 minutes. To halt the reaction, 500 µL of dinitrosalicylic acid (DNSA) reagent was added. The tubes were cooled to room temperature after incubation for five minutes in boiling water.The reaction mixture was diluted with 5 ml of distilled water and absorbance was measured at 540 nm with a spectrophotometer. The blank and controlled were prepared using the same procedure, distilled water for the extract and sodium phosphate buffer for alpha amylase. The α-amylase inhibitory activity was calculated using the % inhibition:

$$\% \text{ inhibition} = (Ac - At) / Ac \times 100$$

Where Ac and At are the absorbance of the control and tests, respectively.

Graphs were used to determine the extract concentrations that resulted in 50% inhibition of enzyme activity (IC50) [16].

2.4 *In Silico* Study Design

2.4.1 Preparation of Ligands

The three dimensional structures of 147 phytochemicals extracting from *Cucurbita maxima* known to have anti-cancer, anti-diabetic activities and controls (Acarbose for diabetes and Bicalutamide, Abiraterone for Pca) were were taken from the PubChem database in sdf

format[17].Next, a virtual screening tool known as PyRx 0.8v with a universal force field (UFF) at 500 steps was used to minimization the ligands' energy and then we used PyRx's open babel tool plugin to convert all phytochemical from sdf format to pdbqt[18].

2.4.2 Target Protein Retrieval and Preparation

The X-ray crystallographic structure of the Androgen Receptor (AR) was obtained from the RCSB protein database using PDB ID 1E3G, and the protein structure related to diabetes was retrieved with PDB ID 4W93[19]. Using the BIOVIA Discovery Studio software 2021 Client, the 3D crystal structures of the selected proteins were prepared by eliminating water molecules, heteroatoms, and ligands[20]. Lastly, the Swiss PDB viewer (spdbv) software v4.1.0 was used to minimize the protein structures.[21]

2.4.3 Molecular Docking

Molecular docking is an effective technique for assessing potential drug molecules guided by receptor proteins for the treatment of disease. A blind docking technique was used to make docking for the selected protein-ligand complexes easier. The Auto-Dock Vina[22] plugin PyRx software was used to molecularly bind the target proteins with the phytocompounds[18].The binding affinity ratings were then used to order the phytocompounds. The top-ranked protein–ligand complexes' molecular interactions were shown using BIOVIA Discovery Studio 2021[23].

2.4.4 Pharmacokinetics and drug-likeness analysis

Preliminary to the molecular docking experiment, the Lipinski Rule and pharmacokinetic characteristics of the designated drugs were assessed using the Swiss ADME online database (https://www.swissadme.ch/)[24]. Among the crucial information included are molecular weight, water solubility, flexibility, polarity, topological polar surface area (TPSA), lipophilicity, pharmacokinetics, drug-likeness, and forecasted safety profile characteristics[25]. Elements of pharmacokinetics (PK) that determine the concentration and behavior of a medicinal substance after delivery. Understanding ADME is essential for effective medicine design and optimization since it influences both safety and effectiveness profiles.[26]

2.4.5 Pharmacokinetics and drug-likeness analysis

A crucial stage in pharmacological research and drug development is evaluating the pharmacokinetic characteristics of possible drug candidates, particularly ADMET (absorption, distribution, metabolism, excretion, and toxicity). The ADMET profiles in this investigation were assessed using pkCSM (https://biosig.lab.uq.edu.au/pkcsm/) [27] and ADMETlab 2.0 (https://lmmd.ecust.edu.cn/admetsar2/result/?tid=742441) . Important factors were examined, including skin sensitivity, hepatotoxicity, AMES mutagenicity, and maximum tolerated dose (MTD). The best compounds were those with good clearance rates and no hepatotoxic or mutagenic qualities. The significance of ADMET predictions in predicting the pharmacokinetic behavior of biomolecules before moving on to preclinical or clinical trials has been shown by earlier research[28].

2.4.6 QSAR and pIC50 Determination

A prominent in the silico approach for determining the bioactivity of novel drugs based on their chemical structure is the quantitative structure-activity relationship (QSAR)[29]. The Chemdesk database was used to calculate the QSAR and pIC50 values using a traditional technique called multiple linear regression (MLR). Quantitative Structure-Activity Relationship (QSAR) models have been used to determine the relationship between a substance's biological activity and its molecular structure. Additionally, QSAR analysis was used as a helpful computational method to forecast the pharmacokinetic behavior, oral bioavailability, and drug-likeness of the chosen bioactive compounds[30].

The following equation has been applied to define the pIC50 activity: 2.7684 + 0.133928895 × (Chiv5) + 1.59986423 × (bcutm1) + 0.02309681 × (MRVSA9) + 0.00671218 × (PEOEVSA5) + 0.002946101 × (MRVSA6) + 0.15963415 × (GATSv4) + 0.207949857 × (J) + 0.082568569 × (Diametert).

2.4.7 Molecular Dynamic Simulation

The conformational stability and dynamic properties of the protein-ligand complexes in the target binding sites were analysed using molecular dynamics (MD) simulations. Simulations were carried out for 100 ns[31]. using the OPLS_3e force field and Desmond v3.6 module

(Schrödinger suite) on Linux environment. The complexes were solvated with TIP3P water in an orthorhombic box with a 10 Å buffer and neutralised with 0.15 M Na^+/Cl^- ions. Production runs were performed under NPT conditions (300 K, 1 atm) using the Nosé–Hoover thermostat and isotropic barostat following energy minimisation and equilibration. Trajectories were saved every 50 ps. After the simulation, several analyses were performed such as RMSD, RMSF, Rg, SASA, MolSA, PSA, and protein ligand interaction using Desmond and Maestro. The simulated complexes were compared to control for relative stability and binding behaviour.

2.4.8 Post simulation MM-GBSA analysis

The binding free energies for the ligand-protein complexes were calculated from the 100 ns MD trajectories using the molecular mechanics generalised Born surface area (MM-GBSA) method [32] using the default settings in the Maestro interface (Schrödinger Release 2020-3).

2.4.9 PCA and DCCM analysis

We used custom-built BioPython programs to perform principal component analysis (PCA) and dynamic cross-correlation matrix (DCCM) studies to explore conformational flexibility, structural changes, and associated residue movements. These investigations give information into binding behaviour, complex stability, protein dynamics and possible allosteric communication channels[33].

2.4.10 Free energy landscape analysis

The stability of phytochemical–protein and control complexes was examined by computing structural compactness, conformational stability and energetically favourable states using RMSD–Rg based free energy landscapes generated from MD trajectories[34]. The computation was done with a self-written Bio-Python script.

2.4.11 Gibbs free energy analysis

A modified Python script based on Boltzmann statistics was used to create Gibbs free energy landscapes, mapping dominating conformational states via PC1 and PC2[35,36].

3. RESULT AND DISCUSSION

3.1 GC-MS Analysis

The chromatograms of *Cucarbita maxima* presented in Figure 8-9 respectively while the identified compounds with their retention time, and peak area (%), are given in *Tables-1* respectably.

3.2 GC-MS Analysis Report of Ethyl Acetate Extract of *C. maxima leaves*

GC-MS analysis identified 74 compounds in the ethyl acetate leaf extract (Table 2) and 92 compounds in the methanolic leaf extract (Table 1) of *Cucurbita maxima.*

***Table 1*:** Bioactive compounds identified in the methanolic leaf extract of *C. maxima*

SL no	COMPOUND	RT	% AREA	COMPOUND NAME
1	CMP01	5.031	0.34	1-Fluorononane
2	CMP02	5.112	0.51	Heptane, 3,4-dimethyl-
3	CMP03	5.406	2.25	2-Propenenitrile, 3-amino-3-phenyl-
4	CMP04	5.459	12.98	2-Propen-1-ol
5	CMP05	5.855	1.69	1,2-Cyclopentanedione, 3-methyl-
6	CMP06	6.016	1.40	3,4,4-Trimethyl-1-penten-3-ol
7	CMP07	6.07	0.25	1-Cyclohexene-1-methanol
8	CMP08	6.191	2.88	Furaneol
9	CMP09	6.32	0.23	2-Methyl-1-ethylpyrrolidine
10	CMP10	6.345	0.18	1-[1,2-Dihydroxy-2-(2-oxopyrrolidin-1-yl)ethyl]-2-pyrrolidinone
11	CMP11	6.369	0.39	N-Allyl-N-ethylformamide
12	CMP12	6.462	1.00	[1,1'-Bicyclopropyl]-2-octanoic acid, 2'-hexyl-, methyl ester
13	CMP13	6.571	0.48	Succinic acid, (4-methoxyphenyl) ester
14	CMP14	6.667	1.43	1-Penten-3-ol
15	CMP15	6.796	0.48	Cyclodecene
16	CMP16	6.921	0.56	2-Octyldodecanol, TMS derivative
17	CMP17	6.962	0.20	2-Octenoic acid, cis-
18	CMP18	7.005	0.37	Piperazine

19	CMP19	7.128	0.42	1-Nitro-2-acetamido-1,2-dideoxy-d-mannitol
20	CMP20	7.201	0.25	Cyclohexanone, 3-methyl-, oxime
21	CMP21	7.245	0.21	2-Ethyl-1-hexyl methylphosphonofluoridate
22	CMP22	7.295	0.14	10-Undecenoic acid, propyl ester
23	CMP23	7.34	0.15	N-Acetyl-L-methionine methyl ester
24	CMP24	7.476	1.10	Pentanedioic acid, ethyl methyl ester
25	CMP25	7.614	0.31	Pentanoic acid, 3-hydroxy-, ethyl ester
26	CMP26	7.701	0.33	dl-Citrulline
27	CMP27	7.811	0.72	Valeric acid, thio-, S-sec-butyl ester
28	CMP28	7.89	0.32	1,3-Oxathiane, 5-isopropyl-2-methyl-
29	CMP29	7.985	0.93	1,4:3,6-Dianhydro-.alpha.-d-glucopyranose
30	CMP30	8.03	1.25	Benzofuran, 2,3-dihydro-
31	CMP31	8.095	0.48	l-Gala-l-ido-octose
32	CMP32	8.149	1.04	2-Pentenoic acid, 4-methyl-, methyl ester
33	CMP33	8.248	0.48	3-Decen-5-yne, 2,2-dimethyl-, (Z)-
34	CMP34	8.305	0.29	4-Methyl-2-mercaptopyridine-1-oxide
35	CMP35	8.365	0.30	Diethyl suberate
36	CMP36	8.42	0.32	1,2-cis-1,5-trans-2,5-dihydroxy-4-methyl-1-(1-hydroxy-1-isopropyl)cyclohex-3-ene
37	CMP37	8.539	0.59	1-Oxaspiro(4,5)decan-2-one
38	CMP38	8.647	0.22	Melezitose
39	CMP39	8.74	0.14	Butenyl tiglate, 3-methyl-2-
40	CMP40	8.814	0.26	1,3:2,5-Dimethylene-4-methyl-d-rhamnitol
41	CMP41	8.95	0.33	(2E,4E)-5-Chloro-3,4-dimethyl-2,4-heptadiene
42	CMP42	8.997	1.69	2-Methoxy-4-vinylphenol
43	CMP43	9.11	0.28	cis-3-Hexenoic acid
44	CMP44	9.175	0.15	2,3-Diazabicyclo[3.2.0]hept-2-ene, 1,6,6,-trifluoro-4-spirocyclopropane-
45	CMP45	9.315	0.10	1,2-Cyclopentanedimethanol, 3-hydroxy-4,4-dimethyl-
46	CMP46	9.375	0.12	Phenol, 2-(ethylthio)-
47	CMP47	9.41	0.13	7-Hydroxymethylbicyclo[2.2.1]heptane-1-carboxylic acid, methyl ester
48	CMP48	9.586	0.38	2,2,2-Trichloro-1-(2-nitrophenylthioamino)ethanol
49	CMP49	9.71	0.48	DL-Proline, 5-oxo-, methyl ester

50	CMP50	9.797	0.18	1-(3,6,6-Trimethyl-1,6,7,7a-tetrahydrocyclopenta[c]pyran-1-yl)ethenone
51	CMP51	9.85	0.20	3-[N'-(3H-Indol-3-ylmethylene)-hydrazino]-5-methyl-[1,2,4]triazol-4-ylamine
52	CMP52	10.65	21.62	1,3-Propanediol, 2-(hydroxymethyl)-2-nitro-
53	CMP53	10.808	6.88	D-Allose
54	CMP54	11.188	0.10	2(4H)-Benzofuranone, 5,6,7,7a-tetrahydro-4,4,7a-trimethyl-, (R)-
55	CMP55	11.334	0.93	3',5'-Dimethoxyacetophenone
56	CMP56	11.6	0.23	Pentanedioic acid, 3,3-dimethyl-, dimethyl ester
57	CMP57	11.689	0.41	.alpha.-D-Glucopyranoside, methyl
58	CMP58	12.055	0.13	3-p-Menthen-7-al
59	CMP59	12.152	0.11	1-Deoxy-d-altritol
60	CMP60	12.623	0.38	1-(2-[3-(2-Acetyloxiran-2-yl)-1,1-dimethylpropyl]cycloprop-2-enyl)ethenone
61	CMP61	13.193	0.27	4-Isopropenyl-4,7-dimethyl-1-oxaspiro[2.5]octane
62	CMP62	13.761	0.43	6-Hydroxy-4,4,7a-trimethyl-5,6,7,7a-tetrahydrobenzofuran-2(4H)-one
63	CMP63	13.89	0.22	2-Cyclohexen-1-one, 4-hydroxy-3,5,6-trimethyl-4-(3-oxo-1-butenyl)-
64	CMP64	14.34	0.32	Neophytadiene
65	CMP65	15.509	0.11	4-Decenoic acid, methyl ester, Z-
66	CMP66	15.582	2.54	Hexadecanoic acid, methyl ester
67	CMP67	15.76	0.11	Andrographolide
68	CMP68	16.396	0.10	(2S,2'S)-2,2'-Bis[1,4,7,10-tetraoxacyclododecane]
69	CMP69	17.238	0.45	Undecanoic acid
70	CMP70	17.987	0.12	2-Propen-1-ol, 3-(2,6,6-trimethyl-2-cyclohexen-1-yl)-
71	CMP71	18.211	0.32	9,12-Octadecadienoic acid, methyl ester, (E,E)-
72	CMP72	18.309	3.16	9,12,15-Octadecatrienoic acid, methyl ester, (Z,Z,Z)-
73	CMP73	18.473	4.74	Phytol
74	CMP74	18.722	0.83	Methyl stearate
75	CMP75	20.725	0.15	Hexanoic acid, 3,7-dimethyl-2,6-octadienyl ester, (E)-
76	CMP76	20.818	1.09	Benzyl .beta.-d-glucoside
77	CMP77	21.025	0.13	.beta.-D-Glucopyranoside, methyl 4,6-O-nonylidene-

78	CMP78	22.021	0.51	Cyclopropanebutanoic acid, 2-[[2-[[2-[(2-pentylcyclopropyl)methyl]cyclopropyl]methyl]cyclopropyl]methyl]-, methyl ester
79	CMP79	24.839	0.25	Methyl 11-docosenoate
80	CMP80	24.987	0.61	Hexadecanoic acid, 2-hydroxy-1-(hydroxymethyl)ethyl ester
81	CMP81	27.8	0.16	1,9-Tetradecadiene
82	CMP82	29.055	5.41	9-Octadecenamide, (Z)-
83	CMP83	29.522	0.22	Squalene
84	CMP84	31.408	0.27	.delta.-Tocopherol
85	CMP85	32.854	0.37	.gamma.-Tocopherol
86	CMP86	33.945	0.66	Vitamin E
87	CMP87	36.661	0.11	Retinal
88	CMP88	37.099	1.85	Stigmasterol
89	CMP89	37.682	0.16	(1R,4aR,4bS,7R,10aR)-1,4a,7-Trimethyl-7-vinyl-1,2,3,4,4a,4b,5,6,7,9,10,10a-dodecahydrophenanthrene-1-carbaldehyde
90	CMP90	38.328	1.00	.beta.-Sitosterol
91	CMP91	38.634	0.32	Desmosterol
92	CMP92	38.775	0.28	9,19-Cyclolanost-24-en-3-ol, (3.beta.)-, TMS derivative

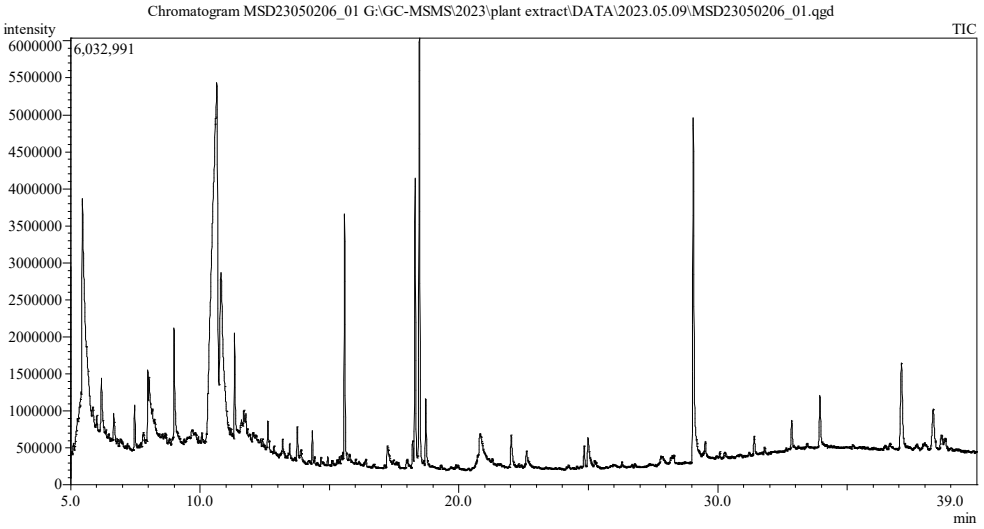


***Figure 1*:** GC-MS chromatogram of methanolic leaf extract of *C. maxima*

***Table2*:** Bioactive compounds identified in the ethyl acetate leaf extract of *C. maxima*

SL No	COMPOUND	RT	% AREA	COMPOUND NAME
1	CMP93	5.03	1.27	Pentanoic acid, 3-methyl-4-oxo-
2	CMP94	5.395	0.19	1-Decene
3	CMP95	5.49	0.10	Decane
4	CMP96	6.607	0.10	Decane, 2,3,5,8-tetramethyl-
5	CMP97	7.632	1.05	Cyclopropane, nonyl-
6	CMP98	7.72	0.47	Dodecane
7	CMP99	8.504	0.10	Dodecane, 2,6,10-trimethyl-
8	CMP100	9.682	1.48	3-Tetradecene, (Z)-
9	CMP101	9.755	0.54	Tridecane
10	CMP102	10.792	0.59	Phenol, 3,5-bis(1,1-dimethylethyl)-
11	CMP103	11.532	1.48	Cetene
12	CMP104	11.601	0.76	.beta.-Allyloxypropionic acid
13	CMP105	12.584	0.51	Dodecyl acrylate
14	CMP106	12.64	0.33	Undecane, 2,4-dimethyl-

15	CMP107	13.865	0.17	Decane, 3,8-dimethyl-
16	CMP108	14.342	1.42	Neophytadiene
17	CMP109	14.945	0.49	3,7,11,15-Tetramethyl-2-hexadecen-1-ol
18	CMP110	16.625	0.59	1-Nonadecene
19	CMP111	18.472	4.47	Phytol
20	CMP112	19.851	0.85	Docosanoic acid, docosyl ester
21	CMP113	23.105	0.23	Acetic acid, chloro-, octadecyl ester
22	CMP114	27.854	0.34	Tritetracontane
23	CMP115	28.35	0.14	Diethylmalonic acid, monochloride, 3,7-dimethyloctyl ester
24	CMP116	29.063	47.51	9-Octadecenamide, (Z)-
25	CMP117	29.305	0.06	trans-2-Hexadecenoic acid
26	CMP118	29.495	4.11	3,5-Decadien-7-yne, 6-t-butyl-2,2,9,9-tetramethyl-
27	CMP119	30.585	0.11	2(1H)-Naphthalenone, 3,4,4a,5,6,7-hexahydro-1,1,4a-trimethyl-
28	CMP120	30.743	1.34	Tetratetracontane
29	CMP121	31.232	0.19	7-Methyl-Z-tetradecen-1-ol acetate
30	CMP122	31.404	1.31	.delta.-Tocopherol
31	CMP123	31.57	0.29	7-(1-Hydroxy-cyclohexyl)-2,2-dimethyl-hept-5-en-3-one
32	CMP124	31.72	0.23	Pentalene, octahydro-2-[(2-octyl)decyl]-

33	CMP125	31.895	0.09	1,1-Dimethyl-3-(3-methyl-1,2,4-oxadiazol-5-yl)guanidine
34	CMP126	32.06	0.10	2- Bromopropionic acid, hexadecyl ester
35	CMP127	32.095	0.10	Cyclohexano[b]thioxan-4-ol, 4-ethyl-2-methyl-, 1,1-dioxide
36	CMP128	32.123	0.14	5,5-Diethyltridecane
37	CMP129	32.313	0.37	9-Undecen-2-one, 6,10-dimethyl-
38	CMP130	32.847	2.43	.gamma.-Tocopherol
39	CMP131	33.355	0.67	10-Chlorodecyl isobutyl carbonate
40	CMP132	33.472	3.82	2-methyloctacosane
41	CMP133	33.575	0.25	Nonadecyl pentafluoropropionate
42	CMP134	33.645	0.10	5-Methyl-Z-5-docosene
43	CMP135	33.855	0.07	Octadecane, 3-ethyl-5-(2-ethylbutyl)-
44	CMP136	33.938	4.37	Vitamin E
45	CMP137	34.139	0.21	.beta.-n-Butylether of 11-epi-dihydroartemisin
46	CMP138	36.205	0.09	4-Hydroxy-.beta.-ionone
47	CMP139	34.799	0.07	1,11-Dibromoundecane
48	CMP140	34.931	0.53	Eicosyl isopropyl ether
49	CMP141	35.115	0.07	1H-imidazole-2-methanol, 1-decyl-
50	CMP142	35.225	0.06	Dihydroartemisinin, 10-O-(t-butyloxy)-
51	CMP143	35.81	0.39	Eicosyl heptyl ether

52	CMP144	35.96	0.33	Hexadecanoic acid, (3-bromoprop-2-ynyl) ester
53	CMP145	38.651	0.67	Ergosta-7,22-dien-3-ol, (3.beta.,22E)-
54	CMP146	36.045	0.17	trans-2-undecenoic acid
55	CMP147	36.085	0.14	6-Nonenal, 3,7-dimethyl-
56	CMP148	37.605	0.54	Vitamin k1(20),heptafluorobutyric deriv.
57	CMP149	36.252	0.14	Tridecane, 5-cyclohexyl-
58	CMP150	36.412	0.18	Decane, 1-bromo-2-methyl-
59	CMP151	36.638	1.15	Nonahexacontanoic acid
60	CMP152	36.78	0.12	Batilol
61	CMP153	36.93	0.07	Ether, dodecyl isopropyl
62	CMP154	37.08	4.87	Stigmasterol
63	CMP155	37.369	0.15	Dimethylmalonic acid, 2-isopropoxyphenyl pentadecyl ester
64	CMP156	37.48	0.14	2,6,10,14-Tetramethyl-7-(3-methylpent-4-enylidene) pentadecane
65	CMP157	37.54	0.09	Cholestan-7-one, cyclic 1,2-ethanediyl acetal, (5.alpha.)-
66	CMP158	34.284	0.06	Butyl 9-hexadecenoate
67	CMP159	37.735	0.26	2- Bromopropionic acid, pentadecyl ester
68	CMP160	38.308	2.46	.beta.-Sitosterol
69	CMP161	36.013	0.21	Octadecanoic acid, 2-hydroxy-, methyl ester
70	CMP162	38.685	0.18	Octadecanenitrile

71	CMP163	38.72	0.35	Chloromethyl undecanoate
72	CMP164	38.757	0.74	cis-1-Chloro-9-octadecene
73	CMP165	39.34	0.09	Dotriacontyl propyl ether
74	CMP166	39.812	0.19	Fumaric acid, 3,5-difluorophenyl dodecyl ester

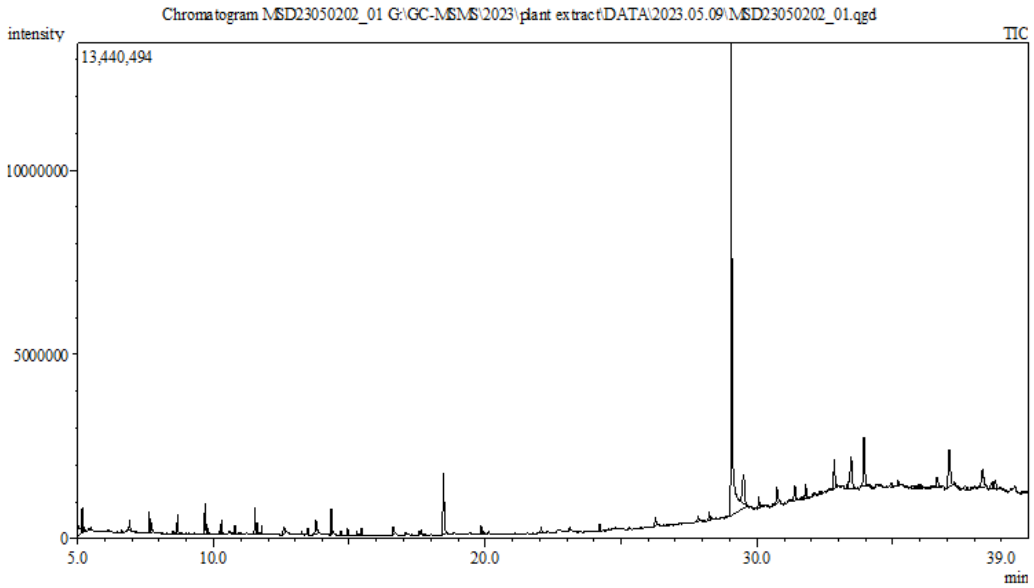


Figure 2: GC-MS chromatogram of ethyl acetate leaf extract of *C. maxima*

3.3 *In-Vitro* Study

3.3.1 Alpha- Amylase Inhibitory Effects

The ability of methanolic leaf extracts of *C. maxima* to suppress the activity of alpha-amylase was examined in the current investigation. These alpha amylase inhibitors are also called as starch blockers since it prevents or slows the absorption of starch into the body mainly by blocking the hydrolysis of 1, 4-glycosidic linkages of starch and other oligosaccharides into maltose, maltriose and other simple sugars [37]. Four different concentrations viz., 1.25, 2.5, 5, and 10 mg/mL of methanolic extract of leaves of *C. maxima* were separately tested for the inhibition of α-amylase activity (*Table 3*). Acarbose was used as reference standard at the same

concentration and values were calculated (Table 4) and compared with α- amylase inhibition of the methanolic extract of *C. maxima* leaves. Log-linear concentration–response relationship, given in Figure 3 for extract and standard compounds, respectively was used to calculate IC50 values. Percent alpha amylase inhibition of the extracts was plotted as a function of concentration in comparison with Acarbose as shown in Figure 3.

Table 3: Absorbance and % Inhibition Data (Mean ± SD)

Concentration (mg/mL)	Test (% inhibition, mean ± SD)	Standard (% inhibition, mean ± SD)
1.25	11.44 ± 6.17	29.91 ± 0.43
2.50	27.06 ± 0.50	39.50 ± 0.21
5.00	48.90 ± 0.16	58.22 ± 0.21
10.00	68.32 ± 0.17	73.27 ± 0.51

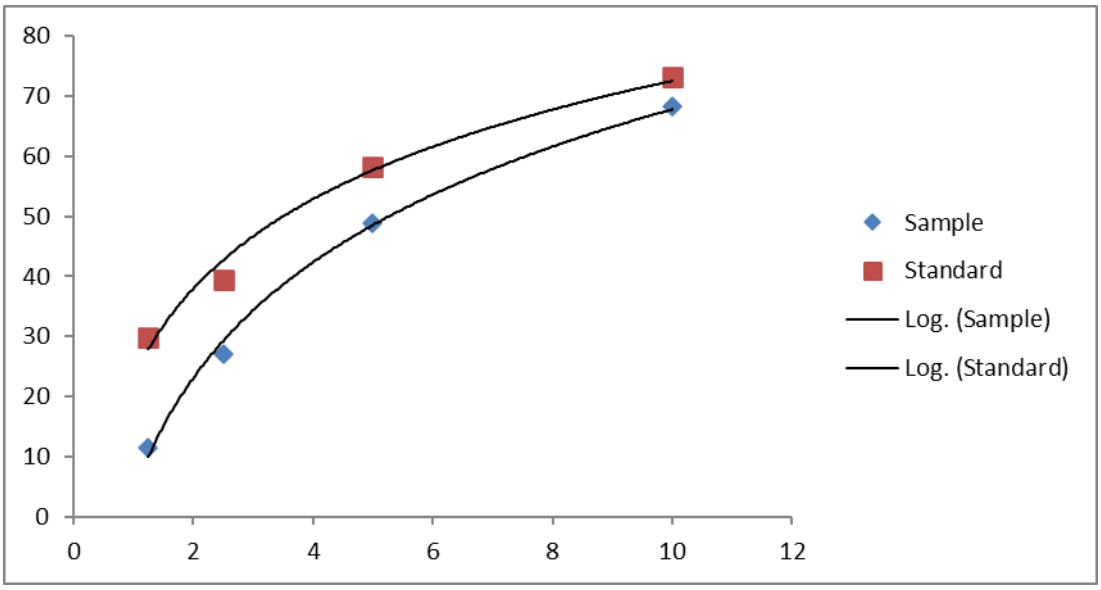


Figure 3: Log-linear concentration–response relationship

Table 4: Regression Parameters and Calculated IC50 Values

Sample	Regression Model	Equation	R2 Value	IC50 (µg/mL)
Test Sample	Log-Linear Fit	y=63.948×log10(x)+3.857	0.9960	5.27
Standard	Log-Linear Fit	y=49.427×log10(x)+23.115	0.9861	3.50

α-amylase activity was inhibited in the test sample in a concentration-dependent manner, rising from 11.44 ± 6.17% at 1.25 mg/mL to 68.32 ± 0.17% at 10 mg/mL (Table 3). The reference standard, which ranged from 29.91 ± 0.43% to 73.27 ± 0.51%, demonstrated greater inhibition at all tested doses (Table 3). Under the current experimental conditions, the test sample's inhibitory effectiveness was lower than the standard's, as indicated by the IC_{50} values estimated from the log-linear concentration–response relationship (Figure 3), which were 5.27 mg/mL for the test sample and 3.50 mg/mL for the standard. This activity is pertinent to the examination of possible antidiabetic effects of plant-derived materials since α-amylase inhibition can delay starch digestion and, as a result, lower the rate of glucose release[5,38].

3.4 *In Silico* Study

3.4.1 Binding Affinities of Identified Compounds

Molecular docking analysis was used to determine the binding affinities of the 147 compounds and standards to two receptors, as shown in the ***Table 5***. A combination of docking score, important binding interactions with active-site residues, and advantageous pharmacokinetic characteristics obtained from in silico studies were used to identify the top-ranked compounds. ***Table 5*** exhibits the highest binding affinities of several specified substances and standard medications to these receptors. CMP148 (CID: 545768) exhibited the highest binding affinity across all targets, notably diabetes (− 9.8 kcal/mol) and Androgen Receptor (− 8.3 kcal/mol) receptors. CMP145 (CID: 91691444) exhibited significant affinity for Diabetes (− 9.6 kcal/mol) and Androgen Receptor (− 8.3 kcal/mol) receptors. CMP91 (439577). exhibited significant affinity for Diabetes (− 9.2 kcal/mol) and Androgen Receptor (− 8.5 kcal/mol) receptors. CMP88

(CID: 5280794) exhibited significant affinity for Diabetes (− 8.9 kcal/mol) and Androgen Receptor (− 8.6 kcal/mol) receptors. Besides, CMP90 (CID: 222284) exhibited significant affinity for Diabetes (− 9.4 kcal/mol) and Androgen Receptor (− 7.9 kcal/mol) receptors. Standard drugs, including Abiraterone, Bicalutamide, and Acarbose, exhibited predicted substantial interactions, thereby validating the computational methodology.

Table 5: Some compounds have the highest binding affinities and standards to two receptors.

SL No.	CID	Compounds	Binding Affinity (Kcal/mol)	
			Androgen Receptor (PDB: 1E3G)	Diabetes (PDB: 4W93)
CMP88	5280794	Stigmasterol	-8.6	-8.9
CMP91	439577	Desmosterol	-8.5	-9.2
CMP148	545768	Vitamin k1(20),heptafluorobutyric deriv	-8.3	-9.8
CMP145	91691444	Ergosta-7,22-dien-3-ol, (3.beta.,22E)-	-8.3	-9.6
CMP90	222284	.beta.-Sitosterol	-7.9	-9.4
CMP51	9600489	3-[N'-(3H-Indol-3-ylmethylene)-hydrazino]-5-methyl-[1,2,4]triazol-4-ylamine	-7.5	-7.5
CMP76	91691733	Benzyl .beta.-d-glucoside	-7.5	-7.2
CMP50	605654	1-(3,6,6-Trimethyl-1,6,7,7a-tetrahydrocyclopenta[c]pyran-1-yl)ethanone	-7.3	-6.6
CMP138	5363700	4-Hydroxy-.beta.-ionone	-7.2	-6.4
CMP67	5318517	Andrographolide	-7.1	-5
CMP87	638015	Retinal	-6.9	-7.2
CMP13	542537	Succinic acid, (4-methoxyphenyl) ester	-6.9	-5

CMP110	87221	Docosanoic acid, docosyl ester	-6.9	-5.4
CMP89	620819	(1R,4aR,4bS,7R,10aR)-1,4a,7-Trimethyl-7-vinyl-1,2,3,4,4a,4b,5,6,7,9,10,10a-dodecahydrophenanthrene-1-carbaldehyde	-6.9	-8.3
CMP63	5371378	2-Cyclohexen-1-one, 4-hydroxy-3,5,6-trimethyl-4-(3-oxo-1-butenyl)-	-6.8	-6.7
	132971	Abiraterone	-8.1	
	2375	Bicalutamide	-7.7	
	9811704	Acarbose		-7.3

3.4.2 Protein-Ligand Interaction

PyMOL and BioVia DiscoveryStudio were used to build drug-protein interactions, hydrogen bonding diagrams, and molecular docking pockets. Hydrophobic interactions (pi-sigma, alkyl, and pi-alkyl), standard and uncommon hydrogen bonds, and donor/acceptor hydrogen bonds were used to study protein–ligand interactions. The way hydrogen and hydrophobic groups interact chemically influences how the drug works.The binding interactions and energy levels of the compounds (CMP88, CMP91, CMP148, CMP145 and CMP90) with the highest binding affinity are shown in Figures 4-12.Different hydrogen-bonding positions are indicated by the green acceptor region and the violet donor region. (Table 6 and 7) includes amino acid residues and bond distances for the greatest binding ligands, such as CMP88, CMP91, CMP148, CMP145 and CMP90 with the targeted protein.

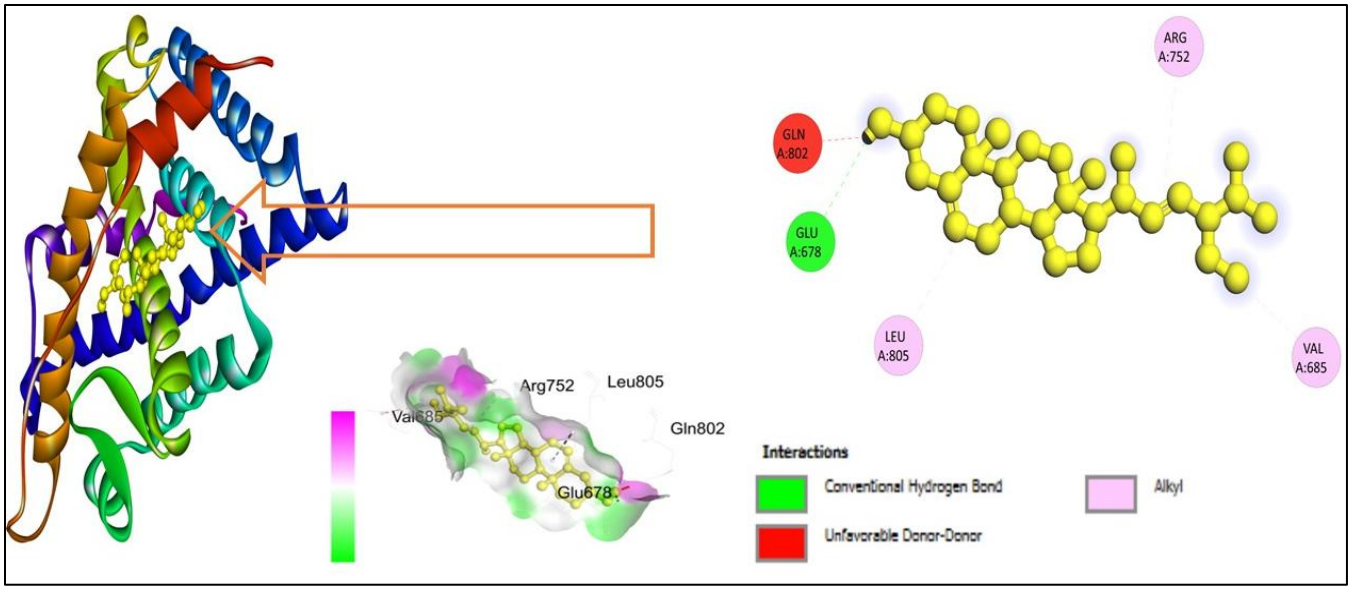


Figure 4: The optimum interaction between the identify ligand (CMP 88) and the PDB: 1E3G receptor within the binding pocket are depicted in 3D and 2D forms.

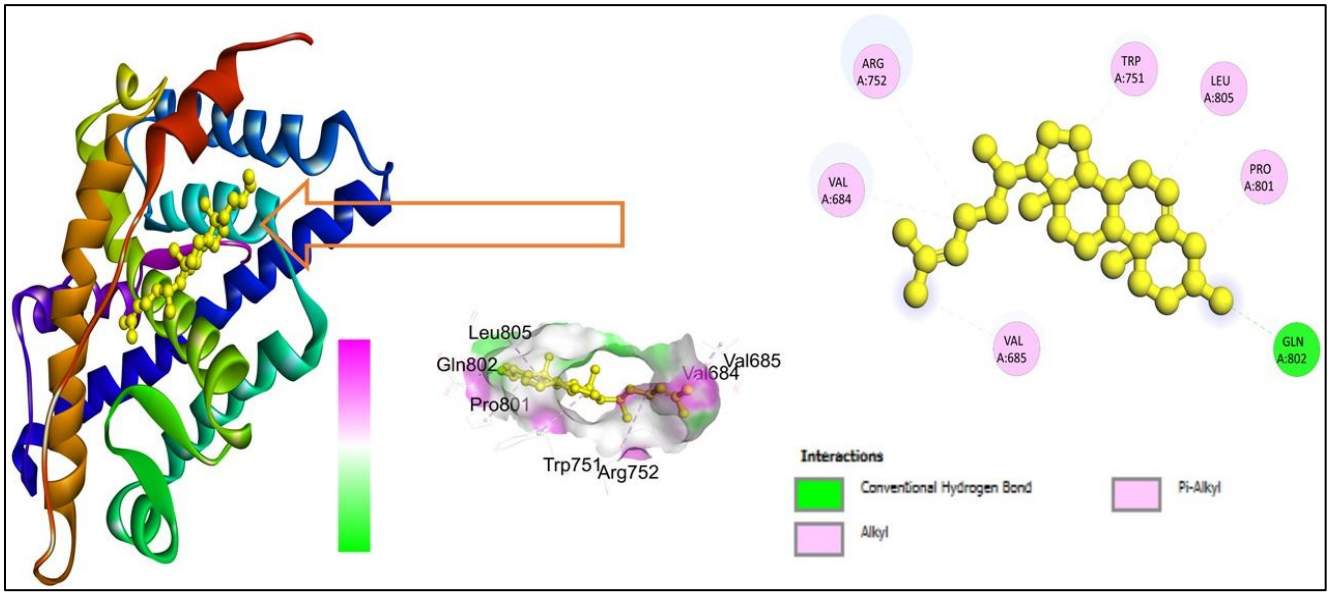


Figure 5: The optimum interaction between the identify ligand (CMP91) and the PDB: 1E3G receptor within the binding pocket are depicted in 3D and 2D forms.

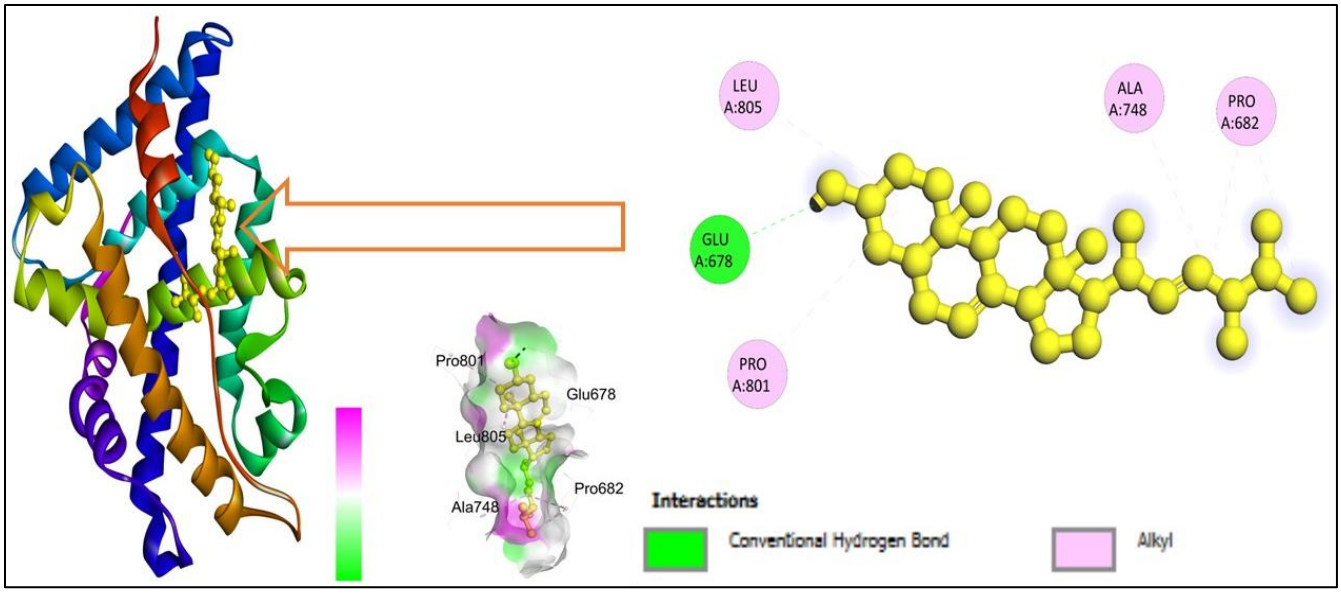


Figure 6: The optimum interaction between the identify ligand (CMP148) and the PDB: 1E3G receptor within the binding pocket are depicted in 3D and 2D forms.

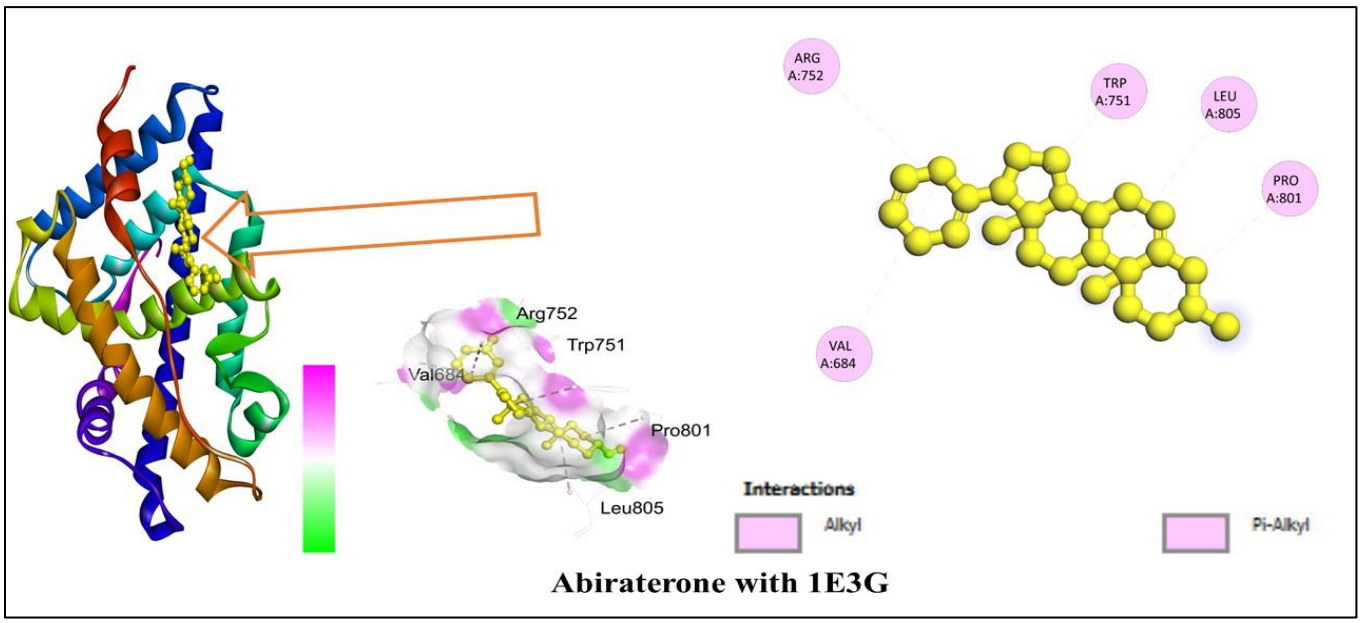


Figure 7: The optimum interaction between the standard Abiraterone and the PDB: 1E3G receptor within the binding pocket are depicted in 3D and 2D forms.

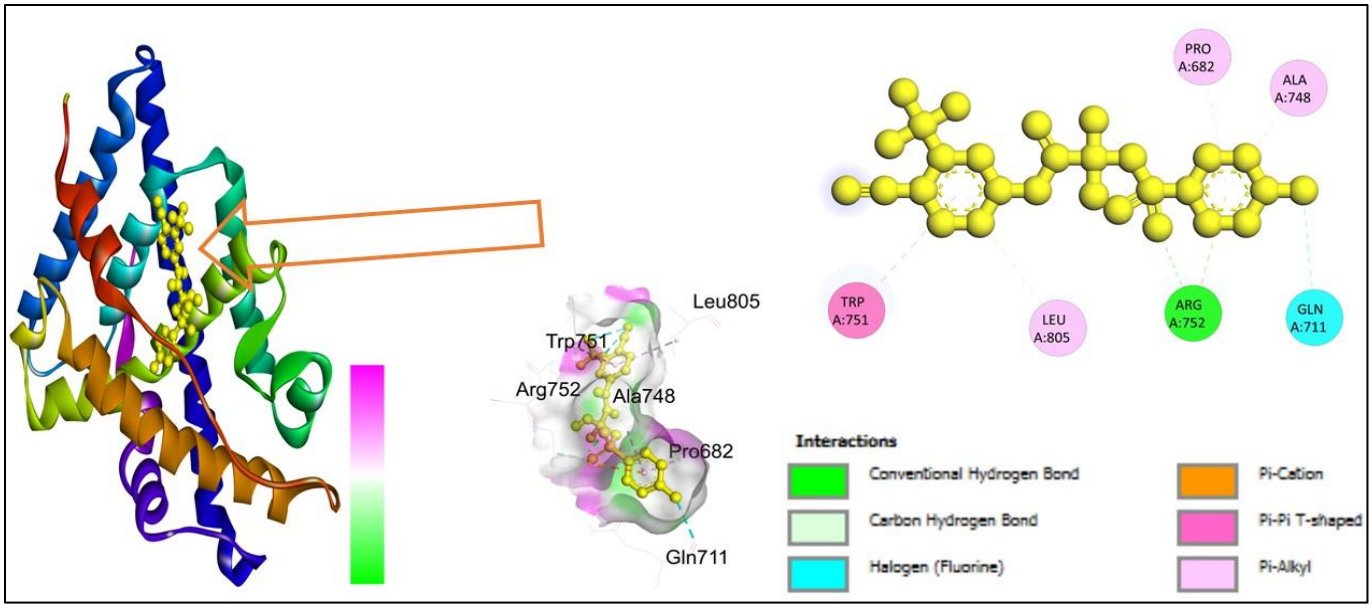


Figure 8: The optimum interaction between the standard Bicalutamide and the PDB: 1E3G receptor within the binding pocket are depicted in 3D and 2D forms.

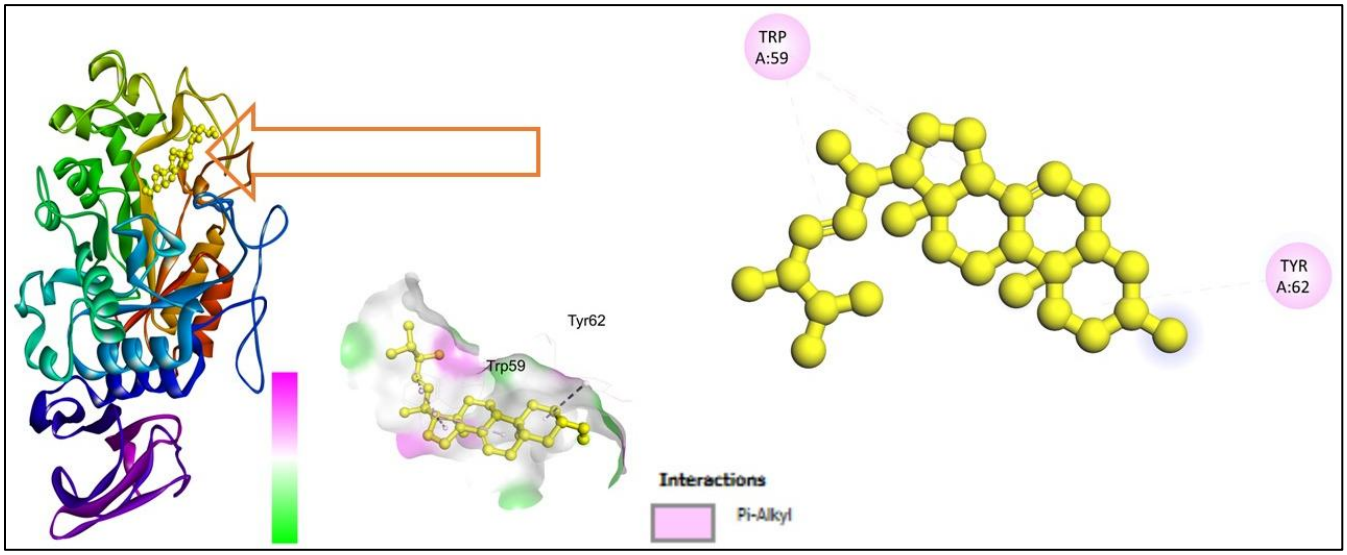


Figure 9: The optimum interaction between the identify ligand (CMP148) and the PDB: 4W93 receptor within the binding pocket are depicted in 3D and 2D forms.

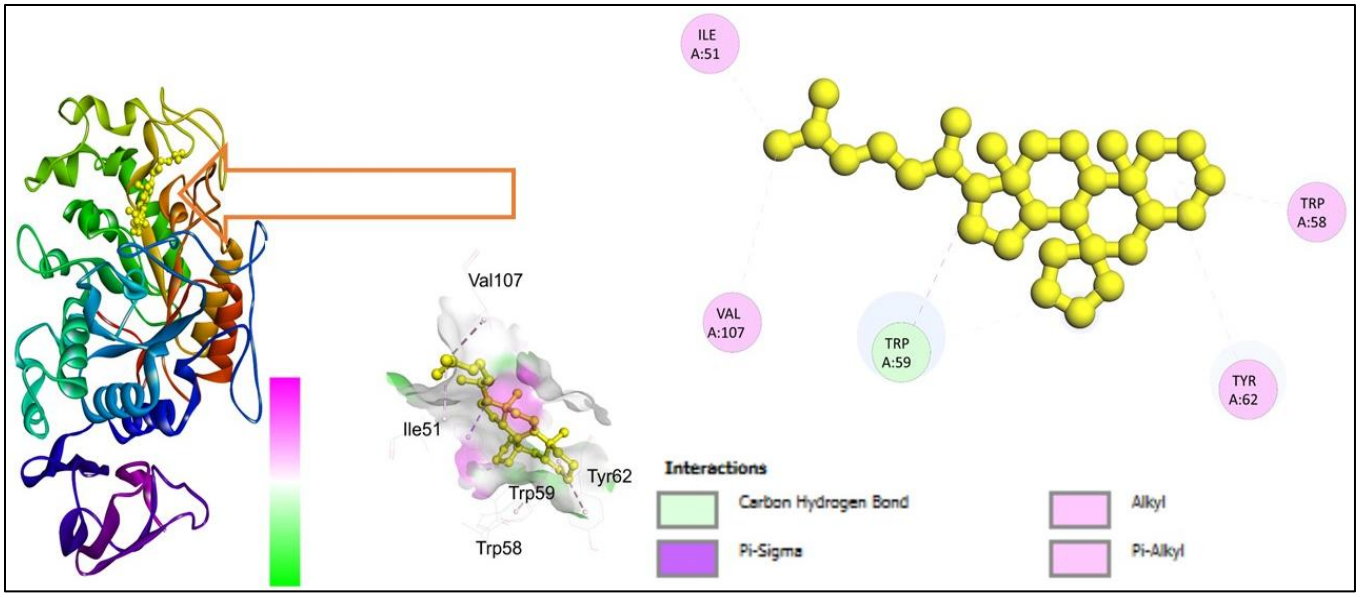


Figure 10: The optimum interaction between the identify ligand (CMP 145) and the PDB: 4W93 receptor within the binding pocket are depicted in 3D and 2D forms.

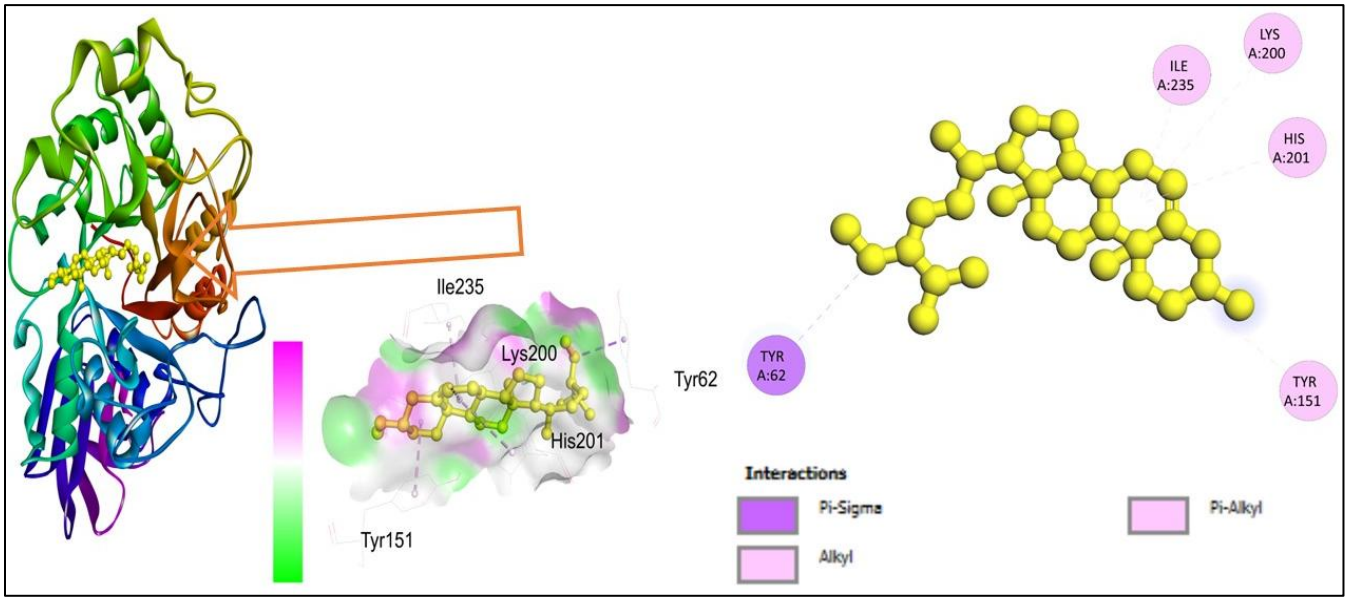


Figure 11: The optimum interaction between the identify ligand (CMP90) and the PDB: 4W93 receptor within the binding pocket are depicted in 3D and 2D forms.



Figure 12: The optimum interaction between the standard Acarbose and the PDB: 4W93 receptor within the binding pocket are depicted in 3D and 2D forms.

***Table 6*:** Ligand interaction with amino acid residues of Androgen Receptor (PDB: 1E3G) and their bond distance

Ligand serial	**CID**	**Docking Score (kcal/mol)**	**Amino Acid (Distances: X)**	**Types**	**Category**
CMP 88	5280794	-8.6	GLU678(2.44805)	Conventional Hydrogen Bond	Hydrogen Bond
			ARG752(4.67245), LEU805(4.91424), VAL685(4.42148)	Alkyl	Hydrophobic
CMP 91	439577	-8.6	GLN802(2.3514)	Conventional Hydrogen	Hydrogen Bond

				Bond	
			VAL684(4.49242), ARG752(4.74331), PRO801(5.47774), LEU805(4.89019), VAL685(4.11142)	Alkyl	Hydrophobic
			TRP751(5.03956)	Pi-Alkyl	
CMP 148	545768	-8.3	GLU678(2.41021)	Conventional Hydrogen Bond	Hydrogen Bond
			PRO682(4.84452), ALA748(4.91394), PRO801(5.3772), LEU805(4.5311), PRO682(4.11457)	Alkyl	Hydrophobic
CMP 145	91691444	-8.3	TRP751(2.16328)	Conventional Hydrogen Bond	Hydrogen Bond
			VAL684(4.80029), ARG752(4.62666), LEU805(4.92487), PRO682(4.07557)	Alkyl	Hydrophobic
CMP 90	222284	-7.9	ALA748(4.81297), ARG752(5.11125), PRO801(5.18353), LEU805(5.29113), VAL685(4.22583)	Alkyl	Hydrophobic

***Table 7*:** Ligand interaction with amino acid residues of Diabetes (PDB: 4W93) and their bond distance

Ligand serial	**CID**	**Docking Score**	**Amino Acid (Distances: X)**	**Types**	**Category**

		(kcal/mol)			
CMP 148	545768	-9.8	TRP59(3.88346), TRP59(5.20423), TRP59(3.75875), TRP59(4.61663), TYR62(5.16558)	Pi-Alkyl	Hydrophobic
CMP 145	91691444	-9.6	TRP59(2.84769)	Carbon Hydrogen Bond	Hydrogen Bond
			TRP59(3.61867)	Pi-Sigma	
			ILE51(3.71152), VAL107(4.08817)	Alkyl	
			TRP58(5.14827), TYR62(5.34891)	Pi-Alkyl	Hydrophobic
CMP 90	222284	-9.4	TYR62(3.74839)	Pi-Sigma	Hydrophobic
			LYS200(5.29448), ILE235(4.16761)	Alkyl	
			TYR151(4.34463), HIS201(5.33379)	Pi-Alkyl	
CMP 91	439577	-9.2	TRP59(3.74839), TRP59(3.73658), TYR62(3.78355)	Pi-Sigma	Hydrophobic
			ALA198(4.97223)	Alkyl	
			TRP59(4.00305), TRP59(4.40111)	Pi-Alkyl	
CMP 88	5280794	-8.9	ILE235(2.65384)	Conventional Hydrogen Bond	Hydrogen Bond

			TYR62(3.69066), TRP59(3.80517)	Pi-Sigma	
			LYS200(4.95101), ILE235(4.71797), ILE235(4.0232), LEU165(4.30788)	Alkyl	
			TRP58(5.22965), HIS201(5.24694), HIS299(4.97647)	Pi-Alkyl	Hydrophobic

3.4.3 Drug-Likeness and Lipinski Rule Assessment

Drug-likeness is the similarity to orally active medications that may be assessed using Lipinski's Rule of Five[39,40].It expects the introduction or inclusion of a molecule when the value of computed logP (ClogP) > 5.37, molecular weight (MW) > 500 g/mol, more than 10 acceptors and more than 5 donors of H-bond[41]. ***Table 8*** Drug-likeness and Lipinski rule properties of selected phytochemicals and standard drugs. The majority of the compounds under study exhibited acceptable drug-like characteristics according to the Lipinski rule of five. Compounds CMP51, CMP76, CMP50, CMP138 and CMP67 revealed no Lipinski violations suggesting good physicochemical qualities for the creation of oral drugs. In contrast, CMP88, CMP91, CMP145 and CMP90 revealed one violation largely owing to greater anticipated lipophilicity (MLOGP > 4.15). CMP148 was violated one time because the molecular weight>500 g/mol. There was one violation for MLOGP with Abiraterone among the reference medications, but Bicalutamide had no violation for Lipinski criterion. Acarbose revealed three breaches, i.e. molecular weight >500 g/mol, high amount of oxygen-containing groups and restrictions on H-bond donor/acceptor and was consequently classed as not fulfilling the Lipinski criterion. In general, the majority of the chosen phytochemicals showed adequate drug-likeness, confirming their potential for future pharmacokinetic and drug-development research. The bioavailability score of all the studied drugs was anticipated as 0.55.

***Table 8*: Lipinski rule characteristics and the drug-likeness of selected compounds**

Compound	CID	Compound Name	Lipinski rule		GI Absorption	BBB	H Bond donor (≤5)	H Bond acceptor (<10)	Consensus Log $P_{o/w}$ (<5)	Log *S* (ESOL)	Molecular weight (g/mol) (< 500)	Bioavailability Score
			Result	Violation								
CMP88	5280794	Stigmasterol	Yes	1 violation: MLOGP>4.15	Low	No	1	1	7.07	-7.46	412.69 g/mol	0.55
CMP91	439577	Desmosterol	Yes	1 violation: MLOGP>4.15	Low	No	1	1	6.69	-7.17	384.64 g/mol	0.55
CMP148	545768	Vitamin k1(20),heptafluorobutyric deriv	Yes	1 violations: MW >500	Low	No	0	10	11.14	-11.59	648.73 g/mol	0.55
CMP145	91691444	Ergosta-7,22-dien-3-ol, (3.beta.,22E)-	Yes	1 violation: MLOGP>4.15	Low	No	1	1	6.62	-6.94	398.66 g/mol	0.55

CMP90	222284	.beta.-Sitosterol	Yes	1 violation: MLOGP>4.15	Low	No	1	1	7.37	-7.90	414.71 g/mol	0.55
CMP 51	9600489	3-[N'-(3H-Indol-3-ylmethylene)-hydrazino]-5-methyl-[1,2,4]triazol-4-ylamine	Yes	0	High	No	2	4	0.83	-2.23	255.28 g/mol	0.55
CMP 76	91691733	Benzyl .beta.-d-glucoside	Yes	0	High	No	1	10	1.51	-2.56	438.43 g/mol	0.55
CMP 50	605654	1-(3,6,6-Trimethyl-1,6,7,7a-tetrahydrocyclopenta[c]pyran-1-yl)ethenone	Yes	0	High	Yes	0	2	2.43	-2.54	206.28 g/mol	0.55
CMP 138	5363700	4-Hydroxy-.beta.-ionone	Yes	0	High	Yes	1	2	2.32	-1.99	208.30 g/mol	0.55
CMP 67	5318517	Andrographolide	Yes	0	High	No	3	5	2.32	-3.18	350.45 g/mol	0.55

	132971	Abiraterone	Yes	1 violation: MLOGP >4.15	High	Yes	1	2	4.50	-5.03	349.51	0.55
	2375	Bicalutamide	Yes	0	Low	No	2	9	3.08	-3.81	430.37 g/mol	0.55
	9811704	Acarbose	No	3 violations: MW >500, NorO>10, NHorOH >5	Low	No	14	19	-6.05	2.57	645.60 g/mol	0.55

3.4.3 Pharmacokinetics and Toxicity

Table 9 summarises the predicted pharmacokinetic and toxicity characteristics of the chosen drugs. In general, majority of the compounds showed good ADME properties associated with drug-likeness. The best expected human intestine absorption was observed for CMP76 (100%), followed by CMP50 (96.82%), CMP90 (95.25%), CMP88 (94.97%), CMP91 (94.46%), and

CMP148 (94.37%). The intestinal absorption of CMP145 and CMP51 were comparably low but nevertheless high i.e. 85.64% and 83.27 % respectively. None of the substances demonstrated the anticipated inhibition of CYP2D6 or CYP3A4 suggesting a limited likelihood for interactions involving these important metabolic enzymes. Likewise, renal OCT2 was anticipated not to be a substrate for all substances. All the chemicals are anticipated to be AMES negative for toxicity, indicating no projected mutagenic activity in AMES model. However, some signs of compound-specific toxicity were detected. The CMP51 and CMP76 were anticipated to be hepatotoxic and the CMP 50 predicted for cutaneous sensitisation. The other chemicals (CMP88, CMP91, CMP148, CMP145, and CMP90) were not predictive for hepatotoxicity or cutaneous sensitisation. The BBB permeability projections were different across the compounds, with CMP90 (0.842), CMP91 (0.781) and CMP88 (0.771) exhibiting significantly greater anticipated permeability, while CMP76 exhibited the lowest value (-1.376). Overall, CMP88, CMP91, CMP148 and CMP90 showed a good balance between high intestine absorption and lack of the investigated toxicity endpoints, encouraging their consideration in further computational and experimental studies. However, these predictions need to be empirically tested before any conclusive conclusions can be drawn concerning safety or pharmacokinetic behaviour. Renal clearance and distribution volumes demonstrated modest systemic stability for the majority of applicants. Standard drugs like acarbose showed notable permeability across the blood-brain barrier, which is consistent with their therapeutic use.

Table 9: Data on pharmacokinetics and toxicity properties obtained from Swiss ADME, admet SAR, and pK CSM online servers

Compound	AMES Toxicity	Absorption		Distribution		Metabolism		Excretion		Toxicity		
		Water solubility Log S	Human Intestinal Absorption (%)	VDss (log L/kg)	BBB Permeability	CYP450 1A2 Inhibitor	CYP450 2D6 Substrate	Total Clearance	Renal OCT2 Substrate	Max. tolerated dose (log mg/kg/day)	Skin Sensitization	Hepatotoxicity
CMP 88	No	-6.682	94.97	0.178	0.771	No	No	0.618	No	-0.664	No	No

CMP 91	No	-6.773	94.464	0.193	0.781	No	No	0.628	No	-0.621	No	No
CMP 148	No	-6.836	94.371	0.423	0.727	No	No	0.61	No	-0.735	No	No
CMP 145	No	-7.029	85.643	0.572	-0.318	No	No	-0.175	No	0.288	No	No
CMP 90	No	-7.397	95.253	0.297	0.842	No	No	0.31	No	-0.424	No	No
CMP 51	No	-2.985	83.272	0.196	0.053	No	No	0.34	No	0.231	No	Yes
CMP 76	No	-3.29	100	-0.283	-1.376	No	No	1.313	No	-0.291	No	Yes
CMP 50	No	-3	96.824	0.282	0.544	No	No	0.076	No	0.512	Yes	No
CMP 138	Yes	-2.583	94.398	0.057	0.123	No	No	1.303	No	0.562	Yes	No
CMP 67	No	-3.494	95.357	-0.286	-0.598	No	No	1.183	No	0.128	No	No
Abiraterone	No	-5.663	96.968	0.884	0.25	No	No	0.486	No	-0.242	No	Yes
Bicalutamide	No	-5.009	77.815	-0.825	-1.154	No	No	0.499	No	0.367	No	Yes

Acarbose	No	-1.361	0	-0.833	-1.841	No	No	0.619	No	0.613	No	No

From ***Table 9***, we could say that these identified compounds have no noticeable toxicity. So, we believe the outcomes will be useful in formulating therapeutic strategies using the traditional medicines, and also the potential hits can be used for further lead optimization for drug discovery.

3.4.4 Analysis of (QSAR) and pIC50

In the context of Quantitative Structure-Activity Relationship (QSAR), PIC50 is the IC50 value's negative logarithm (base 10). It can be used as an accepted metric to convey how well a substance inhibits a certain biological or metabolic activity[42]. Greater potency is indicated by a larger PIC50 value since it correlates with a lower IC50. According to *Table 10*, The QSAR study showed a broad spectrum of expected potency for chosen ligands, with pIC50 values ranging from 4.18 to 6.70. The highest pIC50 result was obtained for CMP148 (CID: 545768) with a value of 6.70, which corresponds to an estimated IC50 of ~0.20 μM, followed by CMP90 (6.37), CMP88 (6.28), CMP145 (6.26) and CMP91 (6.14). Conversely, the CMP51 demonstrated the lowest pIC50 (4.18), suggesting a significantly lower anticipated potency. In general, the compounds with higher pIC50 values had higher values of several structural and physicochemical descriptors, especially PEOE5, molecular surface related metrics and molecular diameter. The greatest values of PEOE5 (96.906), GATS4 (1.55) and molecular diameter (24) were observed for CMP148, indicating that the electronic, topological and size associated properties of this compound may be involved in the expected activity. CMP88 and CMP145 showed very similar descriptor profiles and pIC50 values, further supporting a relationship between the physicochemical properties and the expected potency in this collection of ligands. However, varying numerous descriptors simultaneously makes it difficult to attribute activity to a single molecular characteristic.To summarise, the present QSAR results indicate that CMP148 and other high-pIC50 compounds would be promising candidates for additional research.

***Table 10*: Quantitative structure-activity relationship (QSAR) and pIC50 properties of selected ligands**

SI NO.	CID	Chiv5	bcut m1	(MRV SA9)	(MRVS A6)	(PEOEVS A5)	GATSv 4	J	Diametert	PIC50
CMP 88	5280794	6.542	3.973	0	23.801	65.344	0.566	1.447	15.0	6.28
CMP 91	439577	6.577	3.971	0	23.298	44.069	0.571	1.46	15	6.14
CMP 148	545768	4.244	4.082	16.742	35.392	96.906	1.55	1.55	24	6.70
CMP 145	91691444	6.357	3.977	0	23.801	65.344	0.58	1.458	15	6.26
CMP 90	222284	6.927	3.972	0	11.649	66.033	0.566	1.447	15	6.37
CMP 51	9600489	1.1	3.94	24.065	35.653	18.199	1.018	1.405	11	4.18
CMP 76	91691733	2.492	3.872	23.877	35.895	30.332	1.107	2.393	11	4.54
CMP 50	605654	1.948	3.905	5.783	23.484	19.923	1.01	2.141	6	4.45
CMP 138	5363700	1.137	3.844	5.783	23.298	25.497	1.063	2.589	8	4.53
CMP 67	5318517	3.756	3.919	5.969	23.801	32.076	0.571	1.78	10	5.12

3.5 Molecular Dynamics Simulation

Molecular dynamics (MD) simulations were performed for 100 ns to investigate the structural and dynamic behavior of the selected protein-ligand complexes. The resulting trajectories were analyzed through multiple structural, conformational, and energetic parameters to evaluate the behavior of the complexes throughout the simulation.

3.5.1 Structural Stability and Residue Flexibility

The structural stability and residue-level flexibility of the simulated systems were evaluated using root mean square deviation (RMSD) and root mean square fluctuation (RMSF) analyses over the 100 ns molecular dynamics simulation (Figure 13). The RMSD of protein Cα atoms was calculated to assess the overall deviation of the protein backbone from its reference conformation. RMSD values within the range of 1–3 Å are generally considered acceptable for evaluating protein structural stability during MD simulations [1,2]. For the diabetes target, the apo protein exhibited a mean RMSD of 1.381 ± 0.140 Å, while the CMP88, CMP145, and standard complexes showed mean values of 1.458 ± 0.231 Å, 1.551 ± 0.212 Å, and 1.465 ± 0.245 Å, respectively (Figure 13A). Although CMP88 displayed increased fluctuations at approximately 80–95 ns, reaching a maximum RMSD of 2.21 Å, the trajectory subsequently decreased toward the other systems by the end of the simulation. Overall, the relatively low RMSD values observed for the diabetes systems indicated limited deviation of the protein backbone throughout the simulation. For the prostate cancer target, the apo, CMP88, CMP91, and standard systems exhibited mean RMSD values of 1.414 ± 0.204 Å, 1.780 ± 0.206 Å, 1.267 ± 0.147 Å, and 1.403 ± 0.201 Å, respectively (Figure 13B). Among these systems, CMP91 exhibited the lowest mean RMSD and variability, indicating comparatively limited deviation of the protein backbone from its reference conformation. In contrast, CMP88 showed the highest mean RMSD and a gradual increase during the later simulation period, reaching a maximum of approximately 2.27 Å. Nevertheless, the observed RMSD values remained within the 3 Å criterion, and no persistent large-scale deviation was evident during the 100 ns simulation, supporting the overall structural stability of the investigated systems.

RMSF analysis was subsequently performed to characterize residue-level flexibility. For the diabetes target, the apo, CMP88, CMP145, and standard systems exhibited mean RMSF values of 0.733, 0.828, 0.765, and 0.791 Å, respectively (Figure 13C). Mean fluctuations remained below 1 Å in all systems, indicating generally low flexibility across most residues [3]. Higher

fluctuations were restricted to localized regions. CMP145 showed pronounced fluctuations around residues 306–309, whereas CMP88 exhibited increased flexibility around residues 307–308 and 349–352. The standard complex showed elevated fluctuations around residues 348–351. Notably, the flexible region encompassing residues 349–351 in CMP88 overlapped with the region showing increased fluctuations in the standard complex, whereas the remaining regions of the protein generally exhibited comparatively restricted fluctuations. For the prostate cancer target, mean RMSF values of 0.736, 0.816, 0.792, and 0.712 Å were observed for the apo, CMP88, CMP91, and standard systems, respectively (Figure 13D). CMP91 exhibited comparatively restricted residue-level fluctuations, with no residue exceeding 3 Å and a maximum RMSF of 2.337 Å. In contrast, CMP88 displayed localized increases in flexibility at ASN691, ASN692, and THR918, with THR918 showing the highest fluctuation of 4.028 Å. The standard complex also showed elevated fluctuations at ASN691 and ASN692, indicating that part of the flexible region observed in CMP88 was shared with the standard-bound system. Overall, the RMSD and RMSF profiles demonstrated that the investigated complexes maintained their overall protein conformations during the 100 ns simulations, while the observed increases in flexibility were predominantly confined to specific localized residue regions.

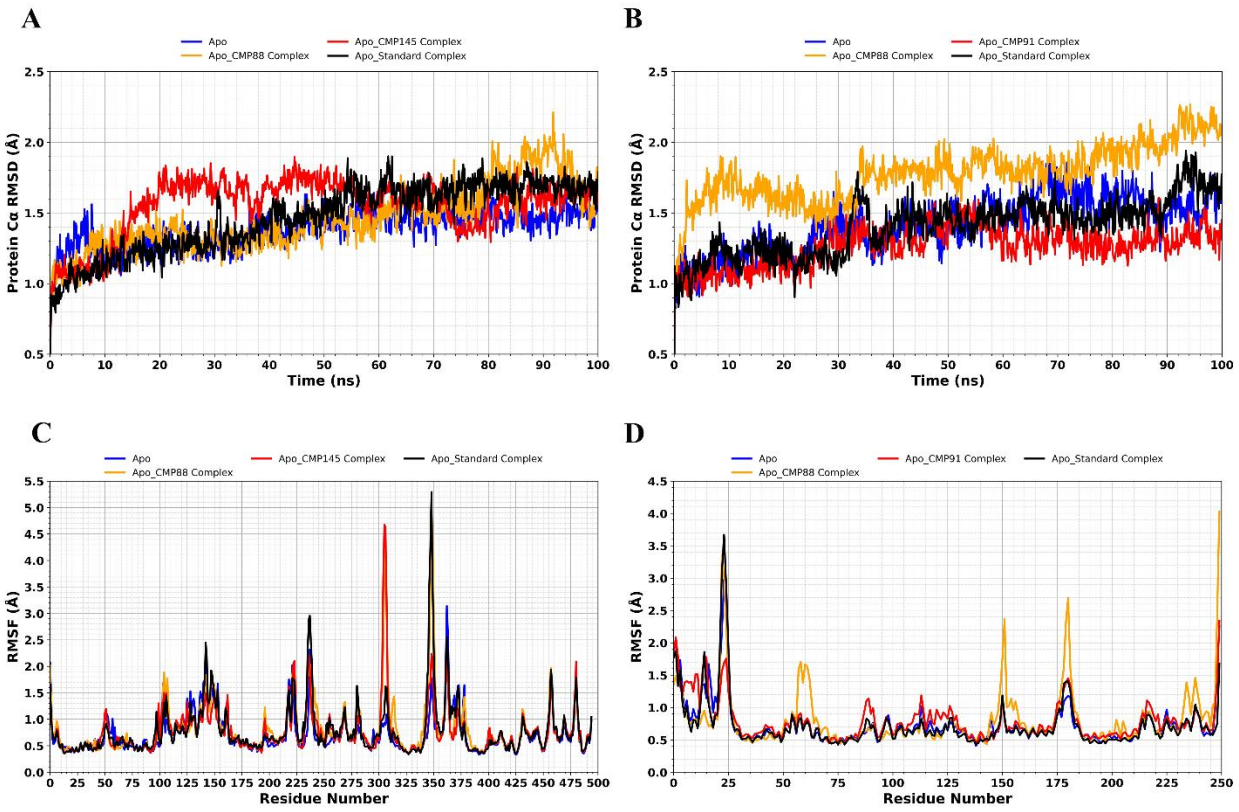


Figure 13. *Structural stability and residue-level flexibility of the investigated protein systems during the 100 ns molecular dynamics simulations. RMSD profiles of the protein Cα atoms for the (A) diabetes and (B) prostate cancer targets, and RMSF profiles showing residue-level fluctuations for the (C) diabetes and (D) prostate cancer targets. The diabetes systems comprise the apo protein, CMP88, CMP145, and standard complexes, whereas the prostate cancer systems comprise the apo protein, CMP88, CMP91, and standard complexes.*

3.5.2 Ligand Conformational Properties and Interaction Profile

The conformational behavior and interaction profiles of the bound ligands during the 100 ns molecular dynamics simulations were further characterized using radius of gyration (Rg), solvent-accessible surface area (SASA), and hydrogen-bond analyses (Figure 14). The Rg was analyzed to assess changes in ligand conformational compactness throughout the simulation [4]. For the diabetes target, CMP88, CMP145, and the standard exhibited mean Rg values of 4.575 ± 0.127, 4.678 ± 0.094, and 5.202 ± 0.103 Å, respectively (Figure 14A). CMP145 exhibited the lowest variation in Rg, indicating comparatively consistent conformational compactness throughout the trajectory. CMP88 showed a gradual increase in Rg after approximately 70 ns,

suggesting a late conformational adjustment of the ligand. The standard maintained a comparatively consistent Rg profile overall, although several transient decreases were observed during the simulation. For the prostate cancer target, CMP88, CMP91, and the standard exhibited mean Rg values of 5.218 ± 0.070, 4.922 ± 0.147, and 4.967 ± 0.328 Å, respectively (Figure 14B). CMP88 showed the lowest variation and maintained a relatively consistent Rg throughout the simulation. CMP91 exhibited moderate variations, including a decrease during approximately 30–55 ns, followed by a comparatively consistent profile during much of the remaining trajectory. In contrast, the standard showed greater Rg variability, including a pronounced transient decrease at approximately 81–88 ns, reaching a minimum of 3.659 Å before returning toward its preceding values. These findings indicate ligand-specific differences in conformational compactness, with CMP145 in the diabetes system and CMP88 in the prostate cancer system showing comparatively consistent Rg profiles.

SASA analysis was subsequently performed to evaluate changes in ligand solvent exposure during the simulation. For the diabetes target, CMP88, CMP145, and the standard showed mean SASA values of 229.07 ± 83.29, 419.85 ± 89.02, and 291.30 ± 21.74 Å², respectively (Figure 14C). CMP88 initially exhibited relatively low solvent exposure but showed a marked increase after approximately 75 ns, consistent with the late conformational adjustment observed in its Rg profile. CMP145 displayed the highest mean SASA and substantial variability, particularly after approximately 20 ns, indicating greater solvent exposure relative to CMP88 and the standard. In contrast, the standard showed the lowest SASA variability and maintained comparatively consistent solvent exposure throughout the simulation. For the prostate cancer target, mean SASA values of 206.31 ± 22.79, 305.19 ± 109.33, and 265.78 ± 39.16 Å² were observed for CMP88, CMP91, and the standard, respectively (Figure 14D). CMP88 exhibited the lowest mean SASA and comparatively limited variation, indicating relatively consistent solvent exposure throughout the trajectory. In contrast, CMP91 showed a pronounced increase in SASA after approximately 55–60 ns, resulting in the highest variability among the three systems and indicating a substantial change in ligand solvent exposure during the latter part of the simulation. The standard displayed moderate fluctuations but remained less variable than CMP91.

Hydrogen-bond analysis was additionally performed to examine the overall hydrogen-bonding network of the simulated systems [5]. For the diabetes target, the apo, CMP88, CMP145, and standard systems exhibited average hydrogen-bond numbers of 465.47 ± 9.21, 463.14 ± 11.60,

461.81 ± 9.69, and 465.27 ± 10.23, respectively (Figure 14E). The trajectories showed substantial overlap, and only minor differences were observed among the average values, indicating that the overall hydrogen-bonding network was largely maintained following ligand binding. For the prostate cancer target, the apo, CMP88, CMP91, and standard systems showed average hydrogen-bond numbers of 253.17 ± 6.47, 243.47 ± 6.99, 253.99 ± 7.46, and 251.18 ± 6.32, respectively (Figure 14F). CMP91 and the standard exhibited average hydrogen-bond numbers comparable to the apo system, whereas CMP88 showed a moderately lower average. Overall, the hydrogen-bond profiles indicate that the hydrogen-bonding network remained relatively consistent across most systems, although a modest reduction was observed for the prostate cancer CMP88 complex.

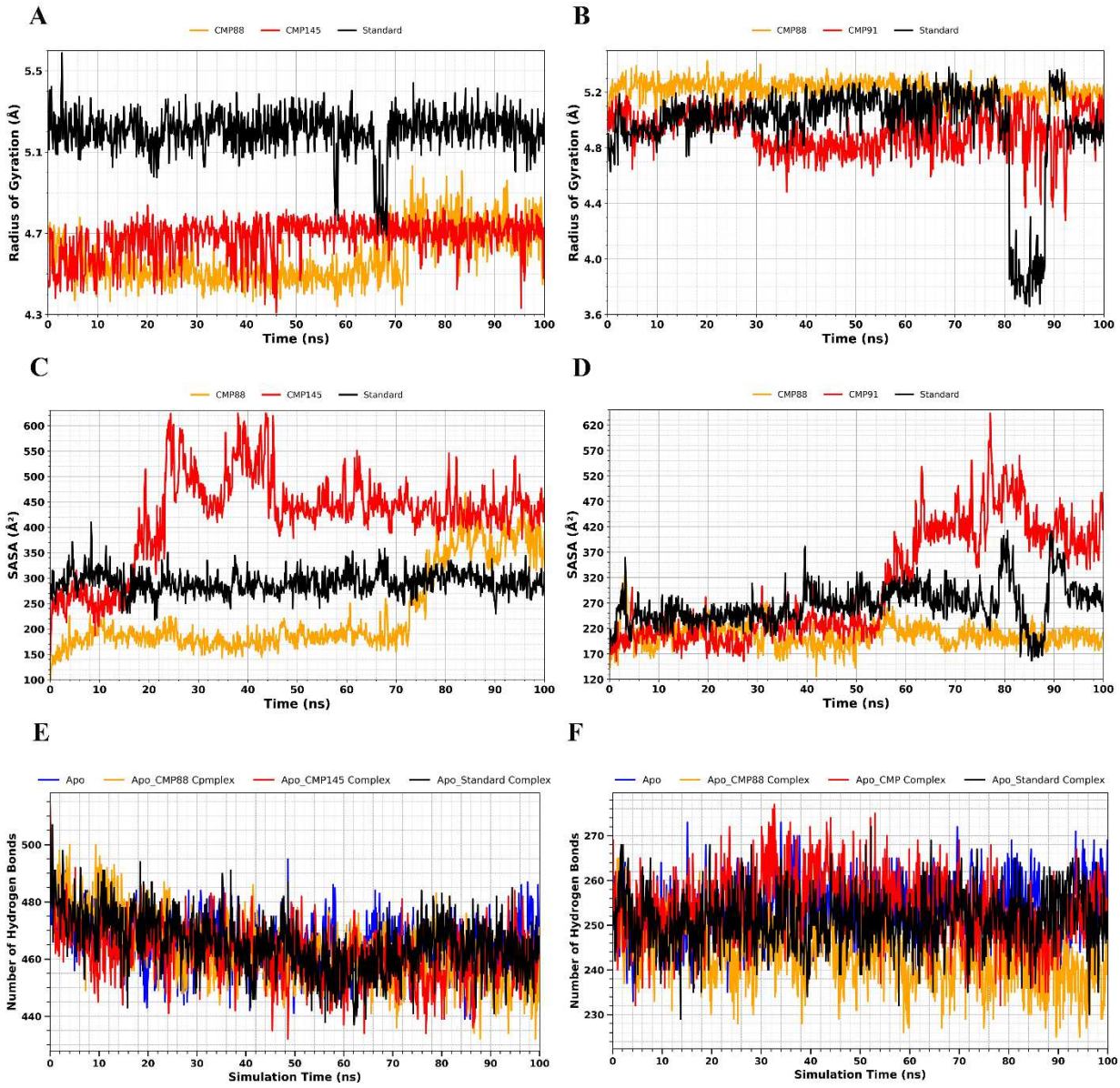


Figure 14. *Ligand conformational properties, solvent exposure, and hydrogen-bonding profiles of the investigated systems during the 100 ns molecular dynamics simulations. Radius of gyration (Rg) profiles of the ligands for the (A) diabetes and (B) prostate cancer targets; solvent-accessible surface area (SASA) profiles of the ligands for the (C) diabetes and (D) prostate cancer targets; and overall hydrogen-bond profiles of the simulated systems for the (E) diabetes and (F) prostate cancer targets. The diabetes ligand-bound systems comprise CMP88, CMP145, and the standard, whereas the prostate cancer ligand-bound systems comprise CMP88, CMP91, and the standard. Apo systems are additionally included in the hydrogen-bond analysis.*

3.5.3 Collective Motion and Correlated Residue Dynamics

Principal component analysis (PCA) and dynamic cross-correlation matrix (DCCM) analysis were performed to characterize the collective conformational motions and correlated residue dynamics of the simulated systems [6]. For the diabetes target, PC1 accounted for 71.79%, 62.37%, 51.56%, and 61.94% of the variance in the apo, CMP88, CMP145, and standard systems, respectively, while PC2 contributed 15.56%, 24.36%, 30.60%, and 26.44%, respectively (Figure 15A–D). Together, PC1 and PC2 represented 87.35%, 86.73%, 82.16%, and 88.38% of the analyzed conformational variance, respectively. The apo system was predominantly governed by PC1, whereas ligand binding redistributed the variance between the first two principal components. CMP145 showed the greatest contribution from PC2 (30.60%) and a comparatively broader distribution across PC1 and PC2, indicating that its conformational variability was distributed more extensively across the two major modes. CMP88 and the standard complex also exhibited altered conformational distributions relative to the apo state, demonstrating ligand-dependent modulation of the collective conformational motions. DCCM analysis further revealed distinct changes in residue–residue dynamic correlations following ligand binding (Figure 15E–H). The apo protein exhibited correlation coefficients ranging from −0.559 to 0.784, indicating the presence of both correlated and anti-correlated residue motions. The corresponding ranges were −0.348 to 0.614 for CMP88, −0.372 to 0.726 for CMP145, and −0.323 to 0.572 for the standard complex. The standard exhibited the lowest dispersion of residue-pair correlations (SD = 0.0645), followed by CMP145 (0.0678), apo (0.0704), and CMP88 (0.0730).

For the prostate cancer target, PC1 explained 60.25%, 58.57%, 43.14%, and 56.41% of the variance in the apo, CMP88, CMP91, and standard systems, respectively, while PC2 accounted for 23.73%, 26.61%, 40.61%, and 24.36%, respectively (Figure 16A–D). Together, PC1 and PC2 represented 83.98%, 85.18%, 83.75%, and 80.77% of the analyzed conformational variance, respectively. Notably, CMP91 exhibited a nearly balanced contribution from PC1 (43.14%) and PC2 (40.61%), indicating that its conformational variability was distributed across two major modes rather than being predominantly governed by PC1. In contrast, the apo, CMP88, and standard systems showed greater contributions from PC1 than PC2. The distinct PC1–PC2 distributions therefore indicate ligand-dependent changes in the collective conformational sampling of the prostate cancer target. Consistent with the PCA findings, DCCM analysis

demonstrated distinct redistribution of correlated residue motions among the prostate cancer systems (Figure 16E–H). The apo protein exhibited correlation coefficients ranging from −0.362 to 0.728. CMP88 showed a broader negative correlation range (−0.558 to 0.698), indicating more pronounced localized anti-correlated motions relative to the apo system. CMP91 displayed the narrowest correlation range (−0.248 to 0.584) and the lowest standard deviation (0.0648), indicating comparatively attenuated correlation amplitudes and a more constrained dynamic correlation profile. The standard complex exhibited correlations ranging from −0.343 to 0.792, with a standard deviation of 0.0662, and showed the strongest positive correlation maximum among the investigated prostate systems. Overall, PCA and DCCM analyses revealed that ligand binding distinctly modulated the collective conformational motions and residue–residue dynamic correlations of the prostate cancer target, with CMP91 displaying a balanced distribution of conformational variance across the first two principal components together with comparatively restricted correlation amplitudes.

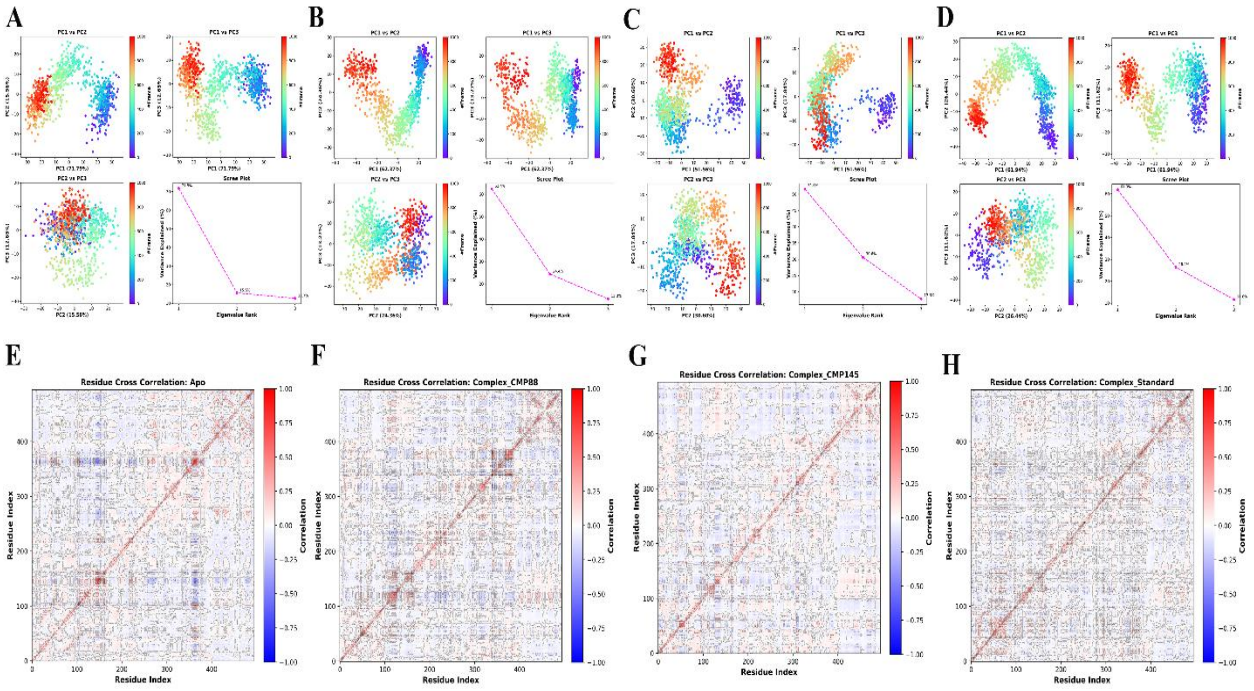


Figure 15. *Principal component analysis (PCA) and dynamic cross-correlation matrix (DCCM) analysis of the diabetes target during the 100 ns molecular dynamics simulation. PC1–PC2 projections of the (A) apo protein, (B) CMP88 complex, (C) CMP145 complex, and (D) standard complex, with the corresponding DCCM maps for (E) apo, (F) CMP88, (G) CMP145, and (H)*

standard systems. In the DCCM maps, positive and negative correlation coefficients represent correlated and anti-correlated residue motions, respectively.

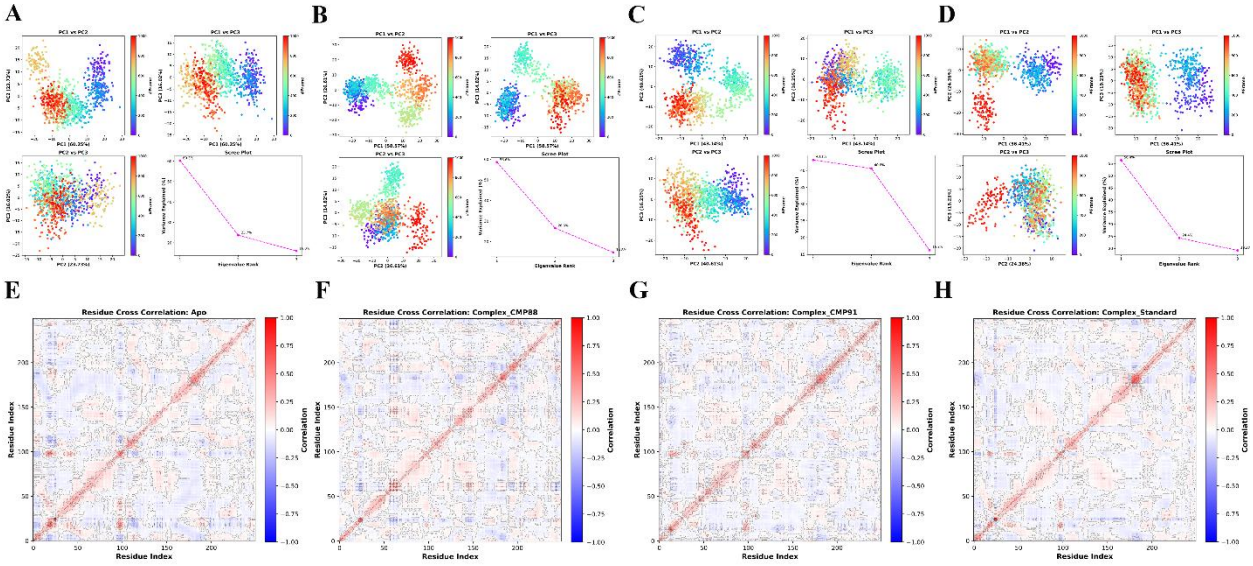


Figure 16. *Principal component analysis (PCA) and dynamic cross-correlation matrix (DCCM) analysis of the prostate cancer target during the 100 ns molecular dynamics simulation. PC1–PC2 projections of the (A) apo protein, (B) CMP88 complex, (C) CMP91 complex, and (D) standard complex, with the corresponding DCCM maps for (E) apo, (F) CMP88, (G) CMP91, and (H) standard systems. Positive and negative correlation coefficients represent correlated and anti-correlated residue motions, respectively.*

3.5.4 Post-Simulation MM/GBSA Binding Energy Analysis

Post-simulation MM/GBSA analysis was performed at selected time points (0, 50, and 100 ns) to estimate the binding energetics of the ligand–protein complexes (Figure 17), while the individual energy components are provided in the Supplementary Material (Tables 11 and 12). For the diabetes target, CMP88 exhibited ΔG_bind values of −32.52, −34.86, and −30.97 kJ/mol at 0, 50, and 100 ns, respectively, showing relatively consistent favorable binding-energy estimates across the three selected snapshots (Figure 17A). CMP145 exhibited corresponding values of −18.84, −31.12, and −35.79 kJ/mol, with progressively more favorable estimates at the later simulation time points. The standard showed ΔG_bind values of −32.61, −25.94, and −37.16 kJ/mol, with its most favorable estimate observed at 100 ns. Energy decomposition revealed that Coulombic and van der Waals interactions were major favorable contributors to the calculated binding

energies, accompanied by additional favorable contributions from hydrogen-bonding, lipophilic, and packing terms. In contrast, the positive generalized Born solvation (Solv_GB) energies opposed binding. For the prostate cancer target, CMP88 exhibited ΔG_bind values of −27.11, −39.96, and −26.56 kJ/mol at 0, 50, and 100 ns, respectively (Figure 17B). The most favorable estimate for CMP88 occurred at 50 ns (−39.96 kJ/mol), which was also the most negative individual ΔG_bind value observed among the investigated prostate complexes at the selected time points. CMP91 showed ΔG_bind values of −21.74, −35.35, and −25.59 kJ/mol, with its most favorable estimate likewise observed at 50 ns. In comparison, the standard exhibited values of −29.21, −24.56, and −35.36 kJ/mol, reaching its most favorable estimate at 100 ns. Energy decomposition similarly indicated substantial favorable contributions from Coulombic and van der Waals interactions, together with contributions from hydrogen-bonding, lipophilic, and packing terms, whereas Solv_GB generally opposed binding. Collectively, the negative MM/GBSA estimates obtained at all three selected time points support energetically favorable ligand–protein association within the MM/GBSA framework, while the variation among snapshots indicates time-dependent differences in the estimated interaction energetics.

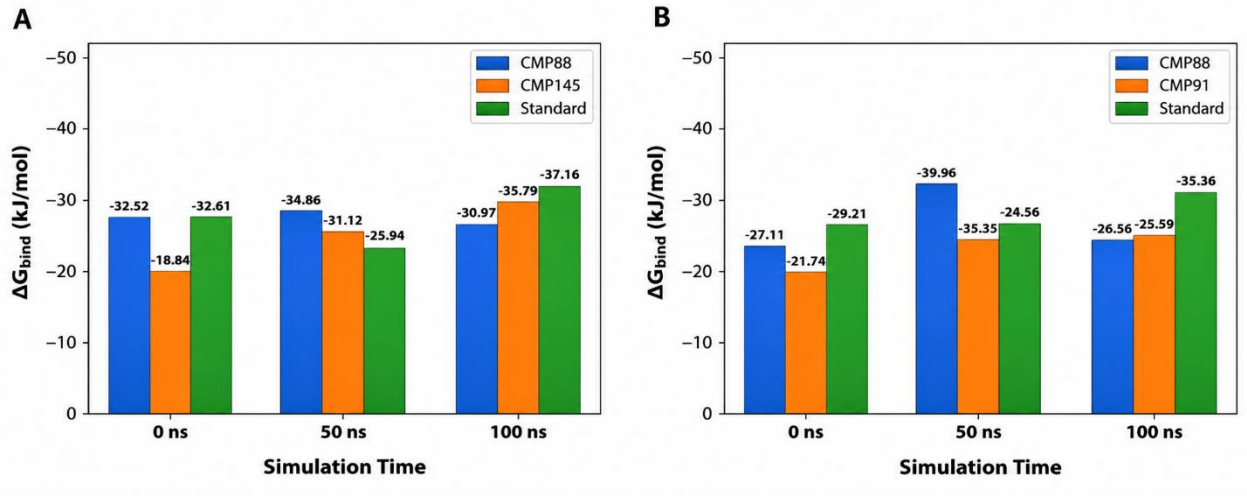


Figure 17. *MM/GBSA binding-energy estimates of the selected compounds and standard at different time points of the 100 ns molecular dynamics simulations. The estimated binding free energies (ΔG_bind) at 0, 50, and 100 ns are presented for (A) the diabetes target (CMP88, CMP145, and standard) and (B) the prostate cancer target (CMP88, CMP91, and standard). More negative ΔG_bind values represent more favorable estimated binding energetics within the MM/GBSA framework.*

Table 11. MM/GBSA binding-energy estimates and individual energy components of CMP88, CMP145, and the standard compound at selected snapshots (0, 50, and 100 ns) from the 100 ns molecular dynamics simulation of the diabetes target.

Ligand	Simulation Time	ΔG_ Bind (kJ/mol)	ΔG_ Bind_ Coulomb (kJ/mol)	ΔG_ Bind_ Covalent (kJ/mol)	ΔG_ Bind_ Hbond (kJ/mol)	ΔG_ Bind_ Lipo (kJ/mol)	ΔG_ Bind_ Packing (kJ/mol)	ΔG_ Bind_ Solv_GB (kJ/mol)	ΔG_ Bind_ vdW (kJ/mol)
CMP88	0 ns	-32.522611	-25.580901	2.577251	-2.106805	-4.325577	-3.163813	16.98432	-19.01331
	50 ns	-34.859939	-12.559302	1.005128	-1.551554	-6.373336	-1.827282	21.764022	-25.284962
	100 ns	-30.974741	-25.988312	3.767604	-1.845134	-4.070949	-1.35224	22.065228	-24.177098
CMP145	0 ns	-18.842395	-15.230951	5.144369	-2.667801	-3.218656	-2.35048	20.351661	-21.404674
	50 ns	-31.12387	-12.867421	-2.594896	-3.102475	-6.031902	-2.357195	16.946924	-28.848204
	100 ns	-35.792888	-25.325744	3.166389	-3.25193	-6.461699	-2.970127	21.264111	-18.739238
Standard	0 ns	-32.61425	-26.295572	-0.22878	-0.742624	-4.702879	-5.271884	25.712664	-23.121015
	50 ns	-25.942619	-25.374775	1.006889	-1.761962	-8.124613	-3.345609	17.299024	-26.616296
	100 ns	-37.158194	-16.95371	0.025323	-1.864637	-0.643309	-2.505719	8.979766	-24.784632

Table 12. MM/GBSA binding-energy estimates and individual energy components of CMP88, CMP91, and the standard compound at selected snapshots (0, 50, and 100 ns) from the 100 ns molecular dynamics simulation of the prostate cancer target.

Ligand	Simulation Time	ΔG_ Bind (kJ/mol)	ΔG_ Bind_ Coulomb (kJ/mol)	ΔG_ Bind_ Covalent (kJ/mol)	ΔG_ Bind_ Hbond (kJ/mol)	ΔG_ Bind_ Lipo (kJ/mol)	ΔG_ Bind_ Packing (kJ/mol)	ΔG_ Bind_ Solv_GB (kJ/mol)	ΔG_ Bind_ vdW (kJ/mol)
CMP88	0 ns	-27.10731	-32.869071	4.193256	-1.146999	-3.860466	-0.765252	14.634702	-24.832328
	50 ns	-39.957682	-41.48082	5.552189	-2.67933	-	-	23.211467	-

						3.246259	2.632606		20.537664
	100 ns	-26.562573	-29.434046	0.407517	-1.588549	-4.470438	-3.165959	16.026188	-24.758319
CMP91	0 ns	-21.743258	-45.185963	-0.57926	-0.361087	-5.913728	-4.007255	22.059485	-23.106504
	50 ns	-35.354414	-14.554786	1.354423	-3.078742	-4.29502	-2.658432	5.633309	-26.195281
	100 ns	-25.590289	-20.137566	2.077528	-0.636213	-2.908908	-2.844981	21.000788	-17.996612
Standard	0 ns	-29.211959	-22.829673	1.711269	-2.115836	-8.717434	-1.979953	23.411578	-24.141665
	50 ns	-24.564461	-26.794718	-0.494146	-1.416888	-5.159456	-0.698219	22.077362	-23.349729
	100 ns	-35.359325	-7.172351	4.712929	-1.547465	-5.211622	-1.080526	18.155047	-22.172663

3.5.5 Free Energy Landscape Analysis

Free energy landscape (FEL) analysis was performed using the radius of gyration (Rg) and root mean square deviation (RMSD) as reaction coordinates to characterize the distribution of energetically favorable conformational states sampled during the 100 ns molecular dynamics simulations (Figure 18). For the diabetes target, the apo protein exhibited a broad and interconnected low-energy region, indicating the sampling of multiple closely related conformational states (Figure 18A). The CMP88 complex displayed a comparatively well-defined dominant low-energy basin, primarily distributed around Rg values of approximately 23.30–23.42 nm and RMSD values of 1.20–1.50 nm (Figure 18B), suggesting preferential sampling of a relatively concentrated conformational region. In contrast, CMP145 exhibited multiple low-energy regions, including a prominent basin at RMSD values of approximately 1.50–1.75 nm and an additional low-energy region around 1.00–1.15 nm (Figure 18C), indicating the presence of distinct energetically accessible conformational states. The standard complex also exhibited an extended and interconnected low-energy landscape encompassing multiple conformational states (Figure 18D).

For the prostate cancer target, the apo protein exhibited a broad and interconnected low-energy landscape encompassing several closely related conformational states (Figure 18E). Ligand binding distinctly redistributed these accessible states. CMP88 showed a shift of the dominant low-energy population toward comparatively higher RMSD values, with the major energetically

favorable region predominantly distributed around RMSD values of approximately 1.50–2.00 nm (Figure 18F). In contrast, CMP91 exhibited a continuous low-energy region primarily distributed at lower RMSD values of approximately 1.05–1.45 nm (Figure 18G). This observation was consistent with the comparatively lower structural deviation observed for CMP91 during the RMSD analysis, indicating that its energetically favorable conformational ensemble was predominantly associated with lower RMSD states. The standard complex displayed a broad and interconnected low-energy region, with prominent favorable states mainly distributed at RMSD values of approximately 1.10–1.60 nm (Figure 18H). Collectively, the FEL analysis revealed ligand-dependent redistribution of the energetically accessible conformational states of the prostate cancer target, with CMP91 preferentially sampling low-energy conformations at comparatively lower RMSD values, whereas CMP88 shifted the dominant low-energy population toward conformations with greater structural deviation.

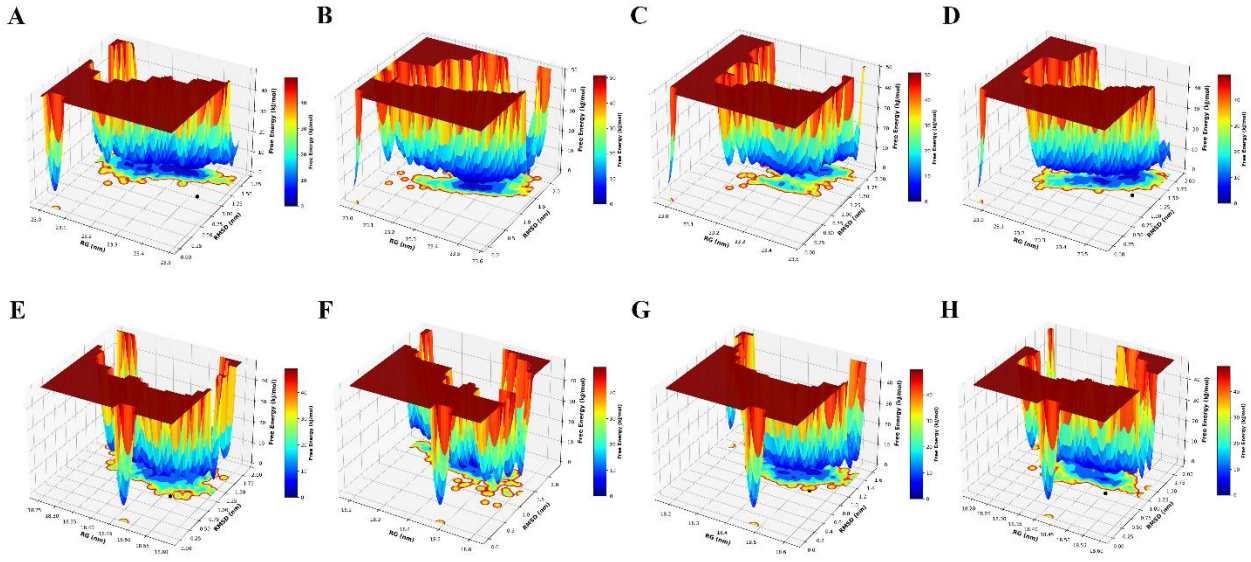


Figure 18. *Free energy landscape (FEL) analysis of the investigated systems during the 100 ns molecular dynamics simulations. FEL maps were constructed using RMSD and radius of gyration (Rg) as reaction coordinates for the diabetes target: (A) apo, (B) CMP88, (C) CMP145, and (D) standard; and the prostate cancer target: (E) apo, (F) CMP88, (G) CMP91, and (H) standard.*

4.1 Conclusion

This study demonstrates integrated *in vitro* and computational evidence for the dual target therapeutic potential for the evaluated plant extract against diabetes and prostate cancer pathways. The extract exhibited concentration- dependent α-amylase inhibition, complemented by molecular docking analysis that identified CMP88 (stigmasterol) and CMP91(desmosterol) as exceptional lead compounds for the diabetes- related target and the androgen receptor, respectively. Subsequent 100-ns molecular dynamics simulations verified the structural integrity and conformational stability of these protein ligand complexes, supported by favorable binding free energy profiles. Collectively, these results suggest CMP88 and CMP91 as promising scaffolds for multi-target drug discovery, paving the way for advanced combinatorial therapeutics. Future endeavors will necessitate comprehensive biochemical, cellular, and *in vivo* validations to confirm their mechanistic precision and therapeutic translational value.

Author Contributions:

S.K.: Conceptualisation, Methodology, Investigation, Writing - Original Draft, Formal Analysis. **M.J.H. & M.A.A.M:** Conceptualisation, Methodology, Validation, Data curation, Writing - original draft. **M.R.H.K.:** Validation, Visualisation, Revised the draft. **M.J.I.P & M.A. R.:** Methodology, & inquiry, **T.S., I.J., M.A. T.J.R. & M.M.H.:**, Formal analysis, & editing. **A.P.S.:** Conceptualisation, Methodology, Validation, Formal analysis, Writing-original draft preparation.

Acknowledgments:

The authors would like to thank all the people and institutions that supported this research.

Funding:

The authors state that no funding or other support was received for this work.

Conflicts of Interest:

The authors declare no conflicts of interest.

Data Availability Statement:

The data supporting the conclusions of this investigation are accessible from the corresponding author on request.

Informed Consent Statement:

Not applicable.

5.1 References

1. Genitsaridi, I. *et al.* 11th edition of the IDF Diabetes Atlas: global, regional, and national diabetes prevalence estimates for 2024 and projections for 2050. *Lancet Diabetes Endocrinol.* **14**, 149-156. (2026).
2. Kahn, S. E. The relative contributions of insulin resistance and beta-cell dysfunction to the pathophysiology of Type 2 diabetes: SE Kahn: Insulin resistance and beta-cell dysfunction. *Diabetologia* **46**, 3-19. (2003).
3. Filho, A. M. *et al.* The GLOBOCAN 2022 cancer estimates: Data sources, methods, and a snapshot of the cancer burden worldwide. *Int. J. Cancer* **156**, 1336–1346 (2025).
4. Nabrdalik, K. *et al.* Gastrointestinal adverse events of metformin treatment in patients with type 2 diabetes mellitus: a systematic review and meta-analysis with meta-regression of observational studies. *BMC Endocr. Disord.* **24**, 206 (2024).
5. Kaur, N. *et al.* Alpha-amylase as molecular target for treatment of diabetes mellitus: A comprehensive review. *Chem. Biol. Drug Des.* **98**, 539–560 (2021).
6. Toeller, M. α-Glucosidase inhibitors in diabetes: efficacy in NIDDM subjects. *Eur. J. Clin. Invest.* **24**, 31-35. (1994).
7. Yee, H. S. & & Fong, N. T. A review of the safety and efficacy of acarbose in diabetes mellitus. *Pharmacother. J. Hum. Pharmacol. Drug Ther.* **16**, 792-805. (1996).

8. Argaev-Frenkel, L. & & Rosenzweig, T. Redox balance in type 2 diabetes: therapeutic potential and the challenge of antioxidant-based therapy. *Antioxidants* **12**, 994. (2023).
9. Obinata, D., Takayama, K., Inoue, S. & & Takahashi, S. Exploring androgen receptor signaling pathway in prostate cancer: A path to new discoveries. *Int. J. Urol.* **31**, 590–597 (2024).
10. Nguyen, P. L. *et al.* Adverse effects of androgen deprivation therapy and strategies to mitigate them. *Eur. Urol.* **67**, 825-836. (2015).
11. Skalicka-Woźniak, K. Natural products in drug discovery: advances and opportunities. *Nat. Rev. Drug Discov.* **20**, 200–216 (2021).
12. Pratama, F. *et al.* Bioactive natural products targeting androgen receptor signaling in prostate cancer: a systematic review. *Cancers* **18**, 786. (2026).
13. Jahan, F. *et al.* Nutritional characterization and antioxidant properties of various edible portions of Cucurbita maxima: A potential source of nutraceuticals. *Heliyon* **9**, (2023).
14. Al-Shaheen, S. J., Kaskoos, R. A., Hamad, K. J. & & Ahamad, J. In-vitro antioxidant and α-amylase inhibition activity of Cucurbita maxima. *J Pharmacogn Phytochem* **2**, 121-124. (2013).
15. Sulastri, E. *et al.* Total phenolic, total flavonoid, quercetin content and antioxidant activity of standardized extract of moringa oleifera leaf from regions with different elevation. *Pharmacogn. J.* **10**, S104–S108 (2018).
16. Kazeem, M. I., Adamson, J. O. & Ogunwande, I. A. Modes of inhibition of α-amylase and α-glucosidase by aqueous extract of morinda lucida benth leaf. *BioMed Res. Int.* **2013**, (2013).

17. Kim, S. *et al.* PubChem 2019 update : improved access to chemical data. **47**, 1102–1109 (2019).
18. Dallakyan, S. & Olson, A. J. Chapter 19 Small-Molecule Library Screening by Docking with PyRx. **1263**, 243–250 (2015).
19. Berman, H. M. *et al.* The Protein Data Bank. **28**, 235–242 (2000).
20. Biovia, D. S. Discovery Studio Visualizer. San Diego.-References. Preprint at (2019).
21. With, G. S., View, D. & Deep, H. O. F. Software review Swiss-PDB Viewer (Deep View). **2**, 195–197 (2001).
22. Trott, O. & Olson, A. J. Software News and Update AutoDock Vina : Improving the Speed and Accuracy of Docking with a New Scoring Function , Efficient Optimization , and Multithreading. https://doi.org/10.1002/jcc (2009) doi:10.1002/jcc.
23. Studio, D. (2015). Dassault systemes BIOVIA, Discovery studio modelling environment, Release 4.5. Accelrys Softw Inc, 98-104.
24. Daina, A., Michielin, O. & Zoete, V. SwissADME : a free web tool to evaluate pharmacokinetics , drug- likeness and medicinal chemistry friendliness of small molecules. *Nat. Publ. Group* 1–13 (2017) doi:10.1038/srep42717.
25. Ã, C. A. L. Lead profiling Lead- and drug-like compounds : the rule-of-five revolution. 337–341 (2004) doi:10.1016/j.ddtec.2004.11.007.
26. Bang, D., Kim, J., Song, H. & Kim, S. ADME-drug-likeness : enriching molecular foundation models via pharmacokinetics-guided multi-task learning for drug-likeness prediction. 352–361 (2025).
27. Muslikh, F. A. *et al.* ADMET Prediction of the Dominant Compound from Mangosteen (Garcinia mangostana L .) using pkCSM : A Computational Approach. **1**, 33–38 (2023).

28. Pires, D. E. V, Blundell, T. L. & Ascher, D. B. pkCSM: Predicting Small-Molecule Pharmacokinetic and Toxicity Properties Using Graph-Based Signatures. https://doi.org/10.1021/acs.jmedchem.5b00104 (2015) doi:10.1021/acs.jmedchem.5b00104.
29. Judge, V. *et al.* Synthesis , Antimycobacterial , Antiviral , Antimicrobial Activity and QSAR Studies of N 2 -acyl isonicotinic Acid Hydrazide Derivatives. 53–76 (2013).
30. Stefaniu, A. & Pirvu, L. C. In Silico Study Approach on a Series of 50 Polyphenolic Compounds in Plants ; A Comparison on the Bioavailability and Bioactivity Data. (2022).
31. Kong, X. *et al.* Calcium-binding properties, stability, and osteogenic ability of phosphorylated soy peptide-calcium chelate. *Front. Nutr.* **10**, 1129548 (2023).
32. Genheden, S. & Ryde, U. The MM/PBSA and MM/GBSA methods to estimate ligand-binding affinities. *Expert Opin. Drug Discov.* **10**, 449–461 (2015).
33. El-Daly, M. M. *et al.* Exploring Echinacea angustifolia for anti-viral compounds against Zika virus RNA-dependent RNA polymerase: a computational study. *Sci. Rep.* **15**, 4060 (2025).
34. Abouzied, A. S. *et al.* Structural and free energy landscape analysis for the discovery of antiviral compounds targeting the cap-binding domain of influenza polymerase PB2. *Sci. Rep.* **14**, 25441 (2024).
35. Ahmed, S. S. & Rahman, M. O. From Flora to Pharmaceuticals: 100 new additions to angiosperms of Gafargaon subdistrict in Bangladesh and unraveling antidiabetic drug candidates targeting DPP4 through in silico approach. *PLOS ONE* **19**, e0301348 (2024).
36. Zhang, X. *et al.* Temperature dependence of the stacking-fault Gibbs energy for Al, Cu, and Ni. *Phys. Rev. B* **98**, 224106 (2018).

37. Jaiswal, P. & Kumar, P. Alpha amylase inhibitory activity of different extract of Terminalia arjuna Bark. *Curr. Trends Biotechnol. Pharm.* **11**, 253–258 (2017).

38. Silveira, D. α-Amylase inhibitors: a review of raw material and isolated compounds from plant source. *J. Pharm. Pharm. Sci.* **15**, 141-183. (2012).

39. LR5.

40. Lipinski, C. A. Lead- and drug-like compounds: the rule-of-five revolution. *Drug Discov. Today Technol.* **1**, 337–341 (2004).

41. Rath, S., Jagadeb, M. & Bhuyan, R. Molecular docking of bioactive compounds derived from Moringa oleifera with p53 protein in the apoptosis pathway of oral squamous cell carcinoma. *Genomics Inform.* **19**, e46 (2021).

42. Dudek, A. Z. Computational Methods in Developing Quantitative Structure-Activity Relationships (QSAR): A Review. 213–228 (2006).